Transient Synchronization Stability of Grid-Tied Multi-VSCs System Considering Nonlinear Damping and Transient Interactions

Zhi Wang, *Graduate Student Member, IEEE*, Li Guo, *Member, IEEE*, Xialin Li, *Member, IEEE*, Zhongguan Wang, *Member, IEEE*, Xiaodi Zang, Jiebei Zhu, *Senior Member, IEEE*, Xu Zhou, and Chengshan Wang, *Senior Member, IEEE*

***Abstract*—This article investigates the phase-locked loop (PLL) synchronization transient stability (PLL-STS) issue of grid-tied multiple voltage source converters (MVSCs) systems, specifically focusing on transient stability evaluation and transient interaction analysis. First, a novel PLL-STS assessment method for MVSCs systems has been proposed, which considers angular frequency jumps, nonlinear damping, and transient interactions among VSCs. Compared with previous studies, this method can accurately evaluate PLL-STS of MVSCs system since the acceleration and deceleration areas of VSCs can be accurately determined by combining equal-area criterion and numerical integration method. Moreover, it can identify the dominant converters which lead to transient instability. Second, by introducing static and dynamic interaction coefficients, influence of static and dynamic interaction on the transient stability of individual converters is quantitatively analyzed. Finally, the theoretical analysis results are verified by PSCAD/ EMTDC time-domain simulation results and RT-LAB hardware-in-the-loop experimental results.**

***Index Terms*—Grid-tied multiple VSCs, phase-locked loop synchronization transient stability (PLL-STS) assessment method, static and dynamic interaction, transient synchronization stability.**

I. Introduction

With the development of renewable energy, voltage source converters (VSCs) are widely applied [1]. Presently, most VSCs employ a phase-locked loop (PLL) to synchronize with the main grid by tracking grid-tied terminal voltage [2], [3]. However, during grid faults, the weakened grid poses a risk of PLL synchronization instability in VSCs, as reported in [4]. Previous works primarily investigated this issue in a single grid-tied VSC system. For example, in [5], [6], [7], and [8], the PLL synchronization stability of the single VSC system was analyzed with the PLL-based second-order model. In [9] and [10], the impact mechanism of current control and dc voltage control on the PLL synchronization stability was revealed using the singular perturbation method. However, the grid-tied multi-VSCs (MVSCs) system presents more intricate challenges. In MVSCs system, the converter terminal voltage is not only influenced by its output current but also by that of other converters, leading to complex transient interactions between converters [11], [12]. The transient interaction can have cascading effects that instability in one converter may trigger instability in others, posing a significant threat to the overall stability of the MVSCs system. Hence, it is essential to analyze the PLL synchronization stability of the MVSCs system.

Existing works on PLL synchronization stability analysis of the MVSCs system are mainly focused on discussing the existence of equilibrium points (EP) in the fault-on state, which had received considerable attention in previous studies [13], [14], [15]. However, even if EP exists during faults, the MVSCs system may still exhibit instability if it cannot reach the fault-on EPs from prefault EPs [16]. Despite this crucial aspect, this remains relatively underexplored in existing literature. Given this gap, this paper concentrates explicitly on the PLL synchronization transient stability (PLL-STS) issue of the MVSCs system, i.e., whether the system can reach the fault-on EPs from prefault EPs.

In addressing the PLL-STS issue of the MVSCs system, two key issues need to be considered: 1) how to evaluate the PLL-STS of the MVSCs system and 2) how the transient interaction affects the PLL-STS of individual converters. In the aspect of transient stability evaluation, previous studies [17], [18], [19], [20] have primarily employed the equal-area criterion (EAC). In [17], [18], an analytical transient stability criterion was developed using the EAC by ignoring the effect of dynamic interaction. However, research [19] points out that dynamic interaction deteriorates the transient stability of the MVSCs system, which needs to be considered. To address this issue, considering the effects of dynamic interaction, a dual-iterative EAC was proposed in [20] to build the stable boundary of the MVSCs system. Note that the dynamic interaction was scaled in [20], which may lead to conservative transient stability assessment results. In addition, studies [17], [18], [19], and [20]

Received 15 April 2024; revised 14 July 2024; accepted 10 August 2024. Date of publication 19 August 2024; date of current version 7 October 2024. This work was supported in part by the National Key R&D Program of China under Project 2023YFB2406700. Recommended for publication by Associate Editor G. De Donato. *(Corresponding authors: Xialin Li; Zhongguan Wang.)*

The authors are with the Key Laboratory of Smart Grid of Ministry of Education, Tianjin University, Tianjin 300072, China (e-mail: 2020234352@tju.edu.cn; liguo@tju.edu.cn; xialinlee@tju.edu.cn; wang_zg@tju.edu.cn; jianzheng@tju.edu.cn; jiebei.zhu@tju.edu.cn; zhouxu@tju.edu.cn; cswang@tju.edu.cn).

Color versions of one or more figures in this article are available at https://doi.org/10.1109/TPEL.2024.3445352.

Digital Object Identifier 10.1109/TPEL.2024.3445352

have not considered the effect of PLL output angular frequency jump when applying EAC to analyze the PLL-STS of the system. Literature [21] indicated that grid faults can cause mutations in the point of common coupling (PCC) voltage, resulting in PLL output angular frequency jumps. In [22], it is pointed out for the first time that the angular frequency jumps in the single grid-tied VSC system can change the equivalent initial kinetic energy of the system, leading to a deterioration in transient stability. Overall, when applying the EAC to analyze the PLL-STS of the MVSCs system, it is crucial to fully consider the effects of angular frequency jumps, nonlinear damping, and transient interactions among converters. However, these factors have not been adequately addressed in [17], [18], [19], and [20].

An alternative approach, using Lyapunov's direct method, was explored in [23] and [24]. In [23], the energy function was constructed, and the domain of attraction of the MVSCs system was obtained using the closest unstable equilibrium point method. However, this approach overlooked the impact of *indefinite* damping on system transient stability, potentially leading to misjudgment in specific scenarios. Furthermore, Fu et al. [24] introduced an extended energy function and derived the Lyapunov stability criterion by the extended invariance principle. Nevertheless, the dynamic interaction term was ignored when deriving the criterion, which may limit the applicability of the method in cases with significant dynamic interaction. Despite these efforts in [17], [18], [19], [20], [21], [22], [23], and [24], there is still a lack of simple and accurate PLL-STS assessment methods for the MVSCs system, which is the first motivation of this article.

Regarding transient interaction analysis, literature [13], [14], and [15] provided foundational qualitative insights into the influence of transient interactions on the PLL-STS of individual converters. To further quantify these insights, Fu et al. [19] and Pal and Panigrahi [24] categorize transient interactions into static interaction and dynamic interaction items. Then, their effects on the PLL-STS of individual converters are analyzed. Notably, in [19], the influence of dynamic interaction items was scaled to its maximum value. However, our research in this article has revealed that this simple scaling method in [19] can sometimes yield misleading conclusions, as it does not adequately capture the variable nature of dynamic interaction. In addition, Fu et al. [24] pointed out that both static and dynamic interactions were harmful to the transient stability of these individual converters. However, from our investigation, dynamic interaction may enhance transient stability in some conditions, which has been validated in this article. To this end, whether the effect of dynamic interaction on PLL-STS of individual converters can be evaluated quantitatively is still an open question, which is another critical motivation of this article.

The contributions of this article are summarized as follows.

1) A novel PLL-STS assessment method for the MVSCs system has been developed, which considers angular frequency jumps, nonlinear damping, and transient interactions among converters. This method can accurately evaluate the transient stability of the MVSCs system since the acceleration and deceleration areas of VSCs can be accurately determined by combining EAC and numerical integration methods. Moreover, it can identify the dominant converters leading to transient instability. Thus, by taking emergency controls, such as temporarily blocking these converters, further deterioration of overall system transient stability can be avoided.
2) Static and dynamic interaction coefficients are introduced to clarify the influence of static and dynamic interactions on the PLL-STS of individual converters. Notably, the dynamic interaction coefficient effectively captures the variable nature of dynamic interaction, which is a critical aspect inadequately addressed in previous research. This capability to accurately represent the variability inherent in dynamic interaction enables a more precise quantitative assessment of its effects on the PLL-STS of individual converters.

The rest of this article is structured as follows. In Section II, a nonlinear model of the MVSCs system is established. In Section III, a novel PLL-STS assessment method is proposed by combining EAC and numerical integration method. The static and dynamic interaction coefficients are introduced to quantitatively evaluate the effect of static and dynamic interaction on the PLL-STS of individual converters. Section IV provides the simulation and RT-LAB hardware-in-the-loop experimental results to validate theoretical analysis. Furthermore, the robustness of the method against parameter uncertainties and the applicability of the method considering voltage-dependent current injection is discussed in Section V. Section VI concludes this article.

II. MVSCs System Modeling

A. System Description

For the multi-VSCs grid-tied system, typical topologies include radial, chain, and hybrid, etc. [25]. In this article, the typical radial topology is chosen as the study scenario to focus on the key innovations of this article without introducing additional complexities. In the typical radial topology, the topology and control structure of the MVSCs system studied in this article are depicted in Fig. 1. This system comprises N converters, each connected to a common PCC via the *LC* filter and line impedance $\boldsymbol{Z_{\mathrm{L}k}}$. These converters are then connected to the infinite bus. Note that these converters have different points of synchronization (POS). In Fig. 1, $\boldsymbol{V_{\mathrm{g}}}$ and $\boldsymbol{V_{\mathrm{t}k}}$ denote the infinite bus and POS_k voltage, respectively. $\boldsymbol{Z_{\mathrm{Lg1}}}$ and $\boldsymbol{Z_{\mathrm{Lg2}}}$ are the equivalent impedance between PCC to fault point and fault point to infinite bus, respectively. $\boldsymbol{Z_{\mathrm{F}}}$ is ground impedance.

In the MVSCs system, each converter is designated by the subscript k, denoted as VSC_k ($k = 12, \ldots, N$). The control strategy for VSC_k during faults consists of two main components: the PLL_k and the current control loop. Specifically, PLL_k performs phase-tracking of the POS_k voltage $\boldsymbol{V_{\mathrm{t}k}}$ to ensure synchronization. It outputs the angular frequency $\omega_{\mathrm{pll}k}$ and phase angle $\theta_{\mathrm{pll}k}$. The relationship between the $\theta_{\mathrm{pll}k}$ and the voltage vector $\boldsymbol{V_{\mathrm{t}k}}$ can be referenced in Appendix A. For the current control, a proportional-integral controller is employed to rapidly regulate the injected current of VSC_k following the current references $I_{\mathrm{t}d\mathrm{ref}k}$ and $I_{\mathrm{t}q\mathrm{ref}k}$.

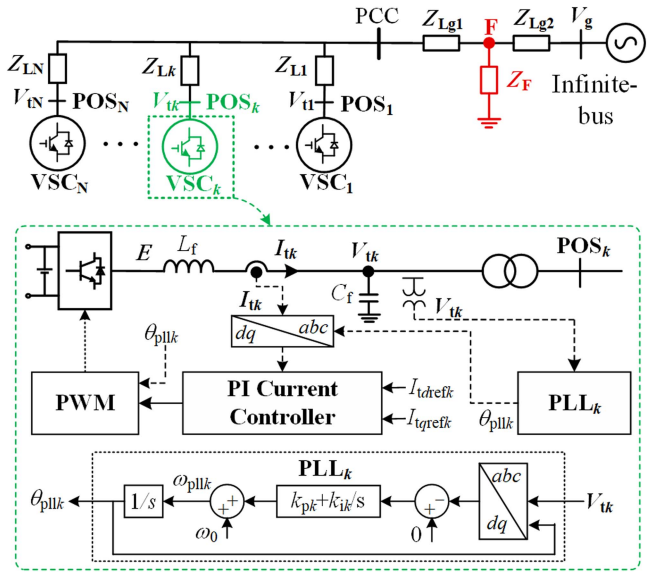

Fig. 1. Topology and control of the MVSCs system.

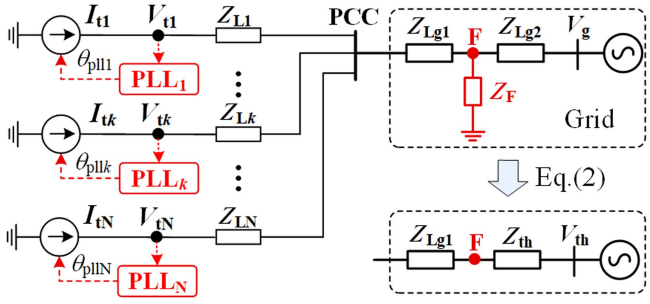

Fig. 2. Equivalent circuit of the MVSCs system.

B. Nonlinear Model of the MVSCs System

This article focuses on exploring the PLL-STS of the MVSCs system within PLL synchronization time scales. To simplify the modeling, the dynamics of the current control are disregarded [14], [15], [16], [17], [18], [19], [20], [21], [22], [23]. This simplification is justified by the fact that the bandwidth of PLL is much lower than that of the current control loop in this study. As a result, the VSC$_k$ can be represented as a current source with an injection current $\boldsymbol{I_{tk}}$, as shown in Fig. 2. The specific expressions for $\boldsymbol{I_{tk}}$ in Fig. 2 are provided in the following equation:

$$\boldsymbol{I_{tk}} = (I_{tdrefk} - jI_{tqrefk})\, e^{j\theta_{pllk}} = I_{trefk} e^{j(\theta_{pllk} - \theta_{Ik})} \tag{1}$$

where $I_{trefk} = \{(I_{t\,drefk})^2 + (I_{t\,qrefk})^2\}^{1/2}$, $\theta_{Ik} = \arctan(I_{t\,qrefk}/I_{t\,drefk})$.

According to Thevenin's theorem, the expressions for $\mathbf{Z_{th}}$ and $\mathbf{V_{th}}$ in Fig. 2 are given in the following equation:

$$\begin{cases} \boldsymbol{V_{th}} = \boldsymbol{V_g Z_F}/(\boldsymbol{Z_F} + \boldsymbol{Z_{Lg2}}) = K_g V_g e^{j(\theta_g + \varphi_g)} \\ \boldsymbol{Z_{th}} = \boldsymbol{Z_{Lg2} Z_F}/(\boldsymbol{Z_F} + \boldsymbol{Z_{Lg2}}) = Z_{th} e^{j\varphi_{th}} \end{cases} \tag{2}$$

where V_g and θ_g are the amplitude and phase of $\boldsymbol{V_g}$, respectively. Z_{th} and φ_{th} are the amplitude and phase of $\mathbf{Z_{th}}$, respectively. The expressions for K_g and φ_g are given in (3). From (3), if the impedance angles of $\mathbf{Z_F}$ and $\mathbf{Z_{Lg2}}$ are equal, then φ_g is equal to zero. Otherwise, φ_g is not equal to zero

$$\begin{cases} K_g = |\boldsymbol{Z_F}/(\boldsymbol{Z_F} + \boldsymbol{Z_{Lg2}})| \\ \varphi_g = \angle(\boldsymbol{Z_F}/(\boldsymbol{Z_F} + \boldsymbol{Z_{Lg2}})). \end{cases} \tag{3}$$

From Fig. 2, the POS$_k$ voltage can be expressed as follows:

$$\boldsymbol{V_{tk}} = \boldsymbol{V_{th}} + (\boldsymbol{Z_{Lk}} + \boldsymbol{Z_{Lg1}} + \boldsymbol{Z_{th}})\, \boldsymbol{I}_{tk} + (\boldsymbol{Z_{Lg1}} + \boldsymbol{Z_{th}}) \sum_{j=1, j\neq k}^{N} \boldsymbol{I}_{tj}. \tag{4}$$

Defining $\mathbf{Z_k} = \mathbf{Z_{Lk}} + \mathbf{Z_{Lg1}} + \mathbf{Z_{th}}$, $\mathbf{Z_e} = \mathbf{Z_{Lg1}} + \mathbf{Z_{th}}$ and combining (2) and (4), then yields the following:

$$\boldsymbol{V_{tk}} = K_g V_g e^{j(\theta_g + \varphi_g)} + Z_k I_{trefk} e^{j(\theta_{pllk} - \theta_{Ik} + \varphi_k)} + Z_e \sum_{j=1, j\neq k}^{N} I_{trefj} e^{j(\theta_{pllj} - \theta_{Ij} + \varphi_e)} \tag{5}$$

where Z_k, Z_e, and φ_k, φ_e are the amplitude and phase of $\mathbf{Z_k}$ and $\mathbf{Z_e}$, respectively.

Transforming $\boldsymbol{V_{tk}}$ to the dq_k coordinate system, the q-axis component of POS$_k$ voltage, denoted as $V_{t\,qk}$, can be obtained as follows:

$$V_{tqk} = K_g V_g \sin(\theta_{pllk} - \theta_g - \varphi_g) + Z_k I_{trefk} \sin(\theta_{Ik} - \varphi_k) + Z_e \sum_{j=1, j\neq k}^{N} I_{trefj} \sin(\delta_{kj} + \theta_{Ij} - \varphi_e) \tag{6}$$

where $\delta_{kj} = \theta_{pll\,k} - \theta_{pll\,j}$, denotes the phase angle difference between PLL$_k$ and PLL$_j$.

The dynamic equation of PLL$_k$ is presented in the following equation:

$$\theta_{pllk} = -\int \left(k_{pk} V_{tqk} + k_{ik} \int V_{tqk} dt + \omega_0 \right) dt \tag{7}$$

where $k_{p\,k}$ and $k_{i\,k}$ are the proportional and integral coefficients of PLL$_k$, respectively.

By combining (6) and (7), we can obtain the nonlinear model for the MVSCs system. To draw on the classical transient synchronous stability analysis theory developed for synchronous generators (SGs), the model of the MVSCs system is rewritten as the form of a swing equation, as formulated in the following equation:

$$\begin{cases} \dot{\delta}_k = \omega_{pllk} - \omega_0 \triangleq \Delta\omega_k \\ J_k \Delta\dot{\omega}_k = P_{mk} - P_{ek} - D_k \Delta\omega_k + P_{ck} \quad k = 1, \ldots, N \\ \Delta\omega_k\,(t_0{}^+) = -k_{pk} V_{tqk}\,(t_0{}^+) \end{cases} \tag{8}$$

where $\delta_k = \theta_{pll\,k} - \theta_g$, denotes the phase angle difference between PLL$_k$ and infinite bus voltage; J_k and D_k are the equivalent inertia and equivalent damping of VSC$_k$, respectively; $P_{m\,k}$ is the equivalent mechanical power of VSC$_k$; $P_{e\,k}$ is the equivalent electromagnetic power between VSC$_k$ and grid; and $P_{c\,k}$ is the equivalent mechanical interactive power between VSC$_k$ and other VSCs, reflecting the impacts of the transient interaction between VSC$_s$ on the VSC$_k$. $\Delta\omega_k(t_0{}^+)$ represents the angular frequency mutation, i.e., at the instant of faults ($t = t_0{}^+$), $\Delta\omega_k$

abruptly jumps from 0 to $-k_{\mathrm{p}k}V_{\mathrm{t}qk}(\mathrm{t}_0{}^+)$; The expressions of J_k, D_k, $P_{\mathrm{m}k}$, $P_{\mathrm{e}k}$, $P_{\mathrm{c}k}$, and $V_{\mathrm{t}qk}(\mathrm{t}_0{}^+)$ are given in the following equation:

$$\begin{cases} J_k = 1/k_{\mathrm{i}k};\ D_k = k_{\mathrm{p}k}K_{\mathrm{g}}V_{\mathrm{g}}\cos(\delta_k-\varphi_{\mathrm{g}})/k_{\mathrm{i}k} \\ P_{\mathrm{m}k} = Z_kI_{\mathrm{tref}k}\sin(\varphi_k-\theta_{Ik});\ P_{\mathrm{e}k} = K_{\mathrm{g}}V_{\mathrm{g}}\sin(\delta_k-\varphi_{\mathrm{g}}) \\ P_{\mathrm{c}k} = \sum_{j=1,j\neq k}^{\mathrm{N}}\begin{bmatrix}-Z_{\mathrm{e}}I_{\mathrm{tref}j}\sin(\delta_{kj}+\theta_{Ij}-\varphi_{\mathrm{e}}) \\ -\frac{k_{\mathrm{p}k}}{k_{\mathrm{i}k}}Z_{\mathrm{e}}I_{\mathrm{tref}j}\cos(\delta_{kj}+\theta_{Ij}-\varphi_{\mathrm{e}})\Delta\omega_{kj}\end{bmatrix} \\ V_{\mathrm{t}qk}(t_0{}^+) \\ = \begin{bmatrix}K_{\mathrm{g}}V_{\mathrm{g}}\sin(\delta_{\mathrm{ke},0}-\varphi_{\mathrm{g}})+Z_kI_{\mathrm{tref}k}\sin(\theta_{Ik}-\varphi_k) \\ +Z_{\mathrm{e}}\sum_{j=1,j\neq k}^{\mathrm{N}}I_{\mathrm{tref}j}\sin(\delta_{kj\mathrm{e},0}+\theta_{Ij}-\varphi_{\mathrm{e}})\end{bmatrix}\end{cases} \tag{9}$$

where $\Delta\omega_{kj} = \Delta\omega_k - \Delta\omega_j$, denotes the angular frequency difference between PLL$_k$ and PLL$_j$; $\delta_{kj\mathrm{e},0} = \delta_{\mathrm{ke},0} - \delta_{j\mathrm{e},0}$, $\delta_{\mathrm{ke},0}$ and $\delta_{j\mathrm{e},0}$ are the prefault relative phase angles of VSC$_k$ and VSC$_j$, respectively.

The synchronous dynamic equation for the muti-SGs system is provided in (B1) and (B2) of Appendix B. From (8) and (B1), the dynamic equations for the MVSCs system and muti-SGs systems exhibit a similar mathematical form. However, comparing (B2) and (9), their synchronization characteristics differ in several aspects.

1) *Angular frequency jumps:* Unlike SGs, where the angular frequency is continuous, the angular frequency $\Delta\omega_k$ of VSC$_k$ exhibits a distinct behavior during faults. Specifically, at the instant of faults ($t = \mathrm{t}_0{}^+$), $\Delta\omega_k$ abruptly jumps to $-k_{\mathrm{p}k}V_{\mathrm{t}qk}(\mathrm{t}_0{}^+)$. This change is attributed to a sudden jump in the q-axis voltage of POS$_k$ when faults occur.
2) *Nonlinear damping:* While the damping of SGs is generally positive, the equivalent damping of VSC$_k$ is nonlinear and may even be negative. Thus, the damping of VSC$_k$ cannot be simply ignored.
3) *Complex transient interaction:* For the multi-SG systems, the transient interaction between SGs is only related to the phase angle difference. However, for the multi-VSCs system, the transient interaction between VSCs involves not only the phase angle difference but also the angular frequency difference, making it more complex.

These differences pose unique challenges in analyzing the PLL-STS for the MVSCs system.

Next, based on the model (8), the PLL-STS for the system during symmetrical faults is analyzed. Note that small-signal stability is the premise for transient stability. Therefore, in addition to the above simplification, the following theoretical analysis and verification ensure that the corresponding EP of the MVSCs system meets the conditions of small-signal stability.

In this article, only symmetrical faults are considered. For asymmetric fault, both positive-sequence (PS) and negative-sequence (NS) synchronization dynamics of the VSCs need to be considered. Moreover, the PS and NS dynamics are coupled between individual VSCs, making the dual-sequence synchronous behavior more complex. However, under asymmetric faults, the PS and NS dynamics of the system can still be described in the form of the swing equation, and thus the PLL-STS can still be analyzed using the methodology proposed in subsection III, which will be provided in our future work.

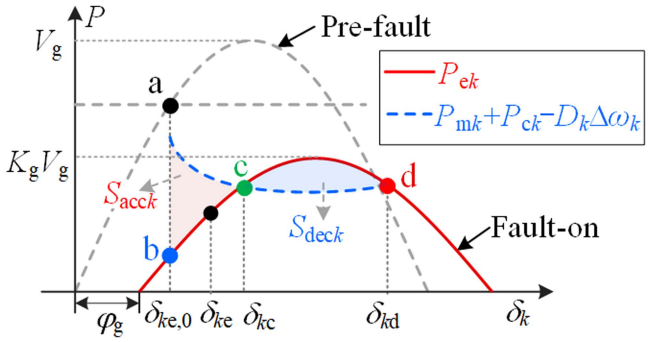

Fig. 3. Acceleration and deceleration area schematic for VSC$_k$.

III. Transient Stability Assessment by Combining EAC and Numerical Integration Methods

Compared to SGs, the synchronization characteristics of the MVSCs system exhibit distinctive features such as angular frequency jumps, nonlinear damping, and complex transient interaction. These unique attributes pose challenges when applying the widely used EAC or extended EAC to evaluate the PLL-STS of the MVSCs system. In this section, a novel approach that combines EAC and numerical integration methods is proposed to evaluate the PLL-STS of the MVSCs system.

In Section III-A, the impacts of nonlinear damping and complex transient interaction between VSCs are considered. Then, with the help of numerical integration methods, we accurately determine the acceleration and deceleration area of VSC$_k$. Then, in Section III-B, considering angular frequency jumps, the PLL-STS criterion for the system is proposed.

Furthermore, in Section III-C, the transient interaction is classified into static and dynamic interaction first. Then, the acceleration and deceleration areas corresponding to static and dynamic interaction are identified. Based on this, the static and dynamic interaction coefficients are introduced to quantitatively analyze the effects of static and dynamic interaction on the PLL-STS of individual VSCs.

A. Calculation of Acceleration and Deceleration Areas of VSC$_k$ by Combining EAC and Numerical Integration Methods

In prefault conditions, VSC$_k$ operates at point a, with an initial phase angle $\delta_{\mathrm{ke},0}$, as depicted in Fig. 3. This section introduces the acceleration and deceleration area of VSC$_k$, exemplified by the case $\delta_{\mathrm{ke}} > \delta_{\mathrm{ke},0}$, where δ_{ke} is the PLL$_k$ phase angle component of the fault-on EP. For subsequent, define $\Delta P_k = P_{\mathrm{m}k} - D_k\Delta\omega_k + P_{\mathrm{c}k} - P_{\mathrm{e}k}$.

After a ground fault occurs, the electromagnetic power curve of VSC$_k$ drops to $P_{\mathrm{e}k}$. The phase angle δ_k does not change abruptly, so the operating point shifts to point b, where $\Delta P_k(\delta_{\mathrm{ke},0}) > 0$. Consequently, VSC$_k$ accelerates from point b to point c. At point c, δ_k reaches the value δ_{kc}, with $\Delta P_k(\delta_{\mathrm{c}k}) = 0$, and $\Delta\omega_k$ reaches its maximum value. During this transient process, the acceleration area of VSC$_k$, denoted as $S_{\mathrm{acc}k}$, can be

calculated as follows:

$$S_{\mathrm{acc}k} = \int_{\delta_{\mathrm{ke},0}}^{\delta_{\mathrm{kc}}} (P_{\mathrm{m}k} - P_{\mathrm{e}k})\, d\delta_k + \int_{\delta_{\mathrm{ke},0}}^{\delta_{\mathrm{kc}}} (P_{\mathrm{c}k} - D_k\Delta\omega_k)\, d\delta_k = f(\delta_{\mathrm{kc}}) - f(\delta_{\mathrm{ke},0}) + g(\delta_{\mathrm{kc}}) \tag{10}$$

where the expressions of $f(\delta_k)$ and $g(\delta_k)$ are as follows:

$$\begin{cases} f(\delta_k) = Z_k I_{\mathrm{tref}k} \sin(\varphi_k - \theta_{Ik})\, \delta_k + K_{\mathrm{g}} V_{\mathrm{g}} \cos(\delta_k - \varphi_{\mathrm{g}}) \\ g(\delta_k) = \int_{\delta_{\mathrm{ke},0}}^{\delta_k} (P_{\mathrm{c}k} - D_k\Delta\omega_k)\, d\delta_k. \end{cases} \tag{11}$$

After crossing point c, where $\Delta P_k < 0$, the VSC$_k$ decelerates and continues to move forward until it reaches point d ($\delta_k = \delta_{kd}$), where the angular frequency $\Delta\omega_k$ decreases to zero or ΔP_k is not less than zero. The deceleration process is completed. The relevant deceleration area, denoted as $S_{\mathrm{dec}k}$, is given by the following equation:

$$S_{\mathrm{dec}k} = \int_{\delta_{\mathrm{kc}}}^{\delta_{\mathrm{kd}}} -(P_{\mathrm{m}k} - P_{\mathrm{e}k})\, d\delta_k + \int_{\delta_{\mathrm{kc}}}^{\delta_{\mathrm{kd}}} -(P_{\mathrm{c}k} - D_k\Delta\omega_k)\, d\delta_k = f(\delta_{\mathrm{kc}}) - f(\delta_{\mathrm{kd}}) + g(\delta_{\mathrm{kc}}) - g(\delta_{\mathrm{kd}}). \tag{12}$$

From (9) to (12), the acceleration and deceleration areas corresponding to the nonlinear damping and the transient interaction term $g(\delta_k)$ are nonintegrable terms. Thus, obtaining analytic expressions for $S_{\mathrm{acc}k}$ and $S_{\mathrm{dec}k}$ is nearly impossible. Most existing studies overlook the damping term and consider the dynamic interaction term constant to derive the acceleration $S_{\mathrm{acc}k}$ and deceleration area $S_{\mathrm{dec}k}$ analytically [15], [17], [18], [19]. However, this approach fails to accurately determine the acceleration and deceleration area, which may lead to conservative PLL-STS assessment results or even misjudge the transient stability of the MVSCs system.

To address this challenge, this article proposes an innovative method that combines EAC and numerical integration methods to precisely calculate the acceleration and deceleration area of VSC$_k$, as depicted in Fig. 4. In Fig. 4, $P_{\mathrm{NI}} = P_{\mathrm{c}k} - D_k\Delta\omega_k$. By accurately determining the acceleration and deceleration areas, the PLL-STS of the MVSCs system can be precisely evaluated, as described in detail in the following section.

B. Transient Stability Assessment for the MVSCs System

Form (8), at the instant of faults ($t = t_0{}^+$), the angular frequency of VSC$_k$ undergoes an instantaneous jump from 0 to $-k_{\mathrm{p}k}V_{tqk}(t_0{}^+)$, denoted as $\Delta\omega_{\mathrm{init}k}$. Thus, the equivalent initial kinetic energy of VSC$_k$ is not equal to zero. Considering the angular frequency jump, the PLL-STS criterion for VSC$_k$ can be described as follows [22]: the sum of the acceleration area and equivalent initial kinetic energy of VSC$_k$ is not greater than its deceleration area. Mathematically, it can be expressed as follows:

$$S_{\mathrm{acc}k} + E_{\mathrm{k0}k} \le S_{\mathrm{dec}k} \tag{13}$$

where $E_{\mathrm{k0}k} = 0.5J_k\Delta\omega_{\mathrm{init}k}{}^2$ represents the equivalent initial kinetic energy of VSC$_k$ due to the angular frequency jump. The jump notably leads to an increase in the acceleration area, consequently degrading the PLL-STS of VSC$_k$. Hence, this factor needs to be considered in the PLL-STS assessment.

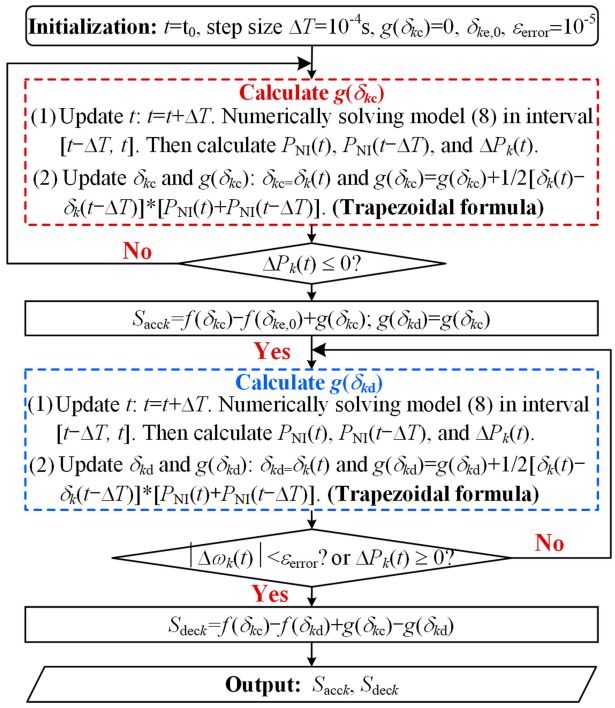

Fig. 4. Flowchart for calculating $S_{\mathrm{acc}k}$ and $S_{\mathrm{dec}k}$.

For the MVSCs system, the dynamics of the converters are coupled with each other. Thus, the MVSCs system can maintain transient stability only when (14) is satisfied, i.e., all converters satisfy the criterion (13)

$$(S_{\mathrm{acc}1} + E_{\mathrm{k}01} \le S_{\mathrm{dec}1}) \cap \cdots \cap (S_{\mathrm{acc}N} + E_{\mathrm{k}0N} \le S_{\mathrm{dec}N}). \tag{14}$$

By combining Fig. 4 and the transient stability criterion (14), the PLL-STS of the MVSCs system can be accurately evaluated. In addition, if any converter, such as the -th converter, fails to meet criterion (13), it not only implies that the MVSCs system is unstable but also identifies the converter as the primary contributor to transient instability. Therefore, using the PLL-STS assessment method proposed in this article, the dominant transient instability converter in the system can also be identified when transient instability occurs.

C. Static and Dynamic Interaction Coefficients

As shown in (9), the transient interactions between VSCs on the VSC$_k$ ($P_{\mathrm{c}k}$) can be classified into two categories: static interaction $P_{\mathrm{cs}k}$ and dynamic interaction $P_{\mathrm{cd}k}$, which are expressed as follows:

$$P_{\mathrm{c}k} = \underbrace{-Z_{\mathrm{e}} \sum_{j=1,j\neq k}^{\mathrm{N}} I_{\mathrm{tref}j} \sin(\delta_{kje} + \theta_{Ij} - \varphi_{\mathrm{e}})}_{P_{\mathrm{cs}k}} + \underbrace{-Z_{\mathrm{e}} \sum_{j=1,j\neq k}^{\mathrm{N}} \left(I_{\mathrm{tref}j} \sin\varphi - \frac{k_{\mathrm{p}k}}{k_{\mathrm{i}k}} I_{\mathrm{tref}j} \cos\varphi \Delta\omega_{kj} \right) - P_{\mathrm{cs}k}}_{P_{\mathrm{cd}k}} \tag{15}$$

where $\varphi = \delta_{kj} + \theta_{Ij} - \varphi_{\mathrm{e}}$.

Substituting (15) into (10) and (12), the transient stability criterion (13) can be further reformulated as follows:

$$\begin{aligned}&\underbrace{\int_{\delta_{\mathrm{ke},0}}^{\delta_{\mathrm{kc}}}\left(P_{\mathrm{m}k}-P_{\mathrm{e}k}-D_k\Delta\omega_k\right)d\delta_k}_{S_{\mathrm{acc}k,1}}+\underbrace{\int_{\delta_{\mathrm{ke},0}}^{\delta_{\mathrm{kc}}}P_{\mathrm{cs}k}d\delta_k}_{S_{\mathrm{acc}k,2}}\\&+\underbrace{\int_{\delta_{\mathrm{ke},0}}^{\delta_{\mathrm{kc}}}P_{\mathrm{cd}k}d\delta_k}_{S_{\mathrm{acc}k,3}}+E_{\mathrm{k}0k}\\&\leq\underbrace{\int_{\delta_{\mathrm{kc}}}^{\delta_{\mathrm{kd}}}-\left(P_{\mathrm{m}k}-P_{\mathrm{e}k}-D_k\Delta\omega_k\right)d\delta_k}_{S_{\mathrm{dec}k,1}}+\underbrace{\int_{\delta_{\mathrm{kc}}}^{\delta_{\mathrm{kd}}}-P_{\mathrm{cs}k}d\delta_k}_{S_{\mathrm{dec}k,2}}\\&+\underbrace{\int_{\delta_{\mathrm{kc}}}^{\delta_{\mathrm{kd}}}-P_{\mathrm{cd}k}d\delta_k}_{S_{\mathrm{dec}k,3}}\end{aligned}\tag{16}$$

where $S_{\mathrm{acc}k,1}$ and $S_{\mathrm{dec}k,1}$ are the acceleration and deceleration areas of VSC$_k$ without transient interaction, respectively. $S_{\mathrm{acc}k,2}$, $S_{\mathrm{acc}k,3}$ and $S_{\mathrm{dec}k,2}$, $S_{\mathrm{dec}k,3}$ represent the acceleration and deceleration areas corresponding to static interaction ($P_{\mathrm{cs}k}$) and dynamic interactions ($P_{\mathrm{ds}k}$), respectively.

Moving $S_{\mathrm{dec}k,2}$ and $S_{\mathrm{dec}k,3}$ to the left side further yields the following:

$$S_{\mathrm{acc}k,1}+\Delta S_{\mathrm{cs}k}+\Delta S_{\mathrm{cd}k}+E_{\mathrm{k}0k}\leq S_{\mathrm{dec}k,1}\tag{17}$$

where $\Delta S_{\mathrm{cs}k}=S_{\mathrm{acc}k,2}-S_{\mathrm{dec}k,2}$, $\Delta S_{\mathrm{cd}k}=S_{\mathrm{acc}k,3}-S_{\mathrm{dec}k,3}$.

In (17), $\Delta S_{\mathrm{cs}k}$ and $\Delta S_{\mathrm{cd}k}$ can be regarded as the effects of static and dynamic interaction on the acceleration area of VSC$_k$, respectively. Thus, $\Delta S_{\mathrm{cs}k}$ and $\Delta S_{\mathrm{cd}k}$ reflect the impact of static and dynamic interaction between VSCs on the PLL-STS of the VSC$_k$, respectively.

To quantitatively assess the effect of static and dynamic interaction between VSCs on the PLL-STS of the VSC$_k$, the article introduces the static and dynamic interaction coefficients, denoted as $\lambda_{\mathrm{s}k}$ and $\lambda_{\mathrm{d}k}$, respectively

$$\begin{cases}\lambda_{\mathrm{s}k}=\Delta S_{\mathrm{cs}k}\\ \lambda_{\mathrm{d}k}=\Delta S_{\mathrm{cd}k}.\end{cases}\tag{18}$$

If $\lambda_{\mathrm{s}k}$ (static interaction) or $\lambda_{\mathrm{d}k}$ (dynamic interaction) is greater than zero, it indicates that the corresponding interactions increase the accelerating area of VSC$_k$, thereby impairing the PLL-STS of VSC$_k$. Conversely, if $\lambda_{\mathrm{s}k}$ or $\lambda_{\mathrm{d}k}$ is less than zero, it suggests that the respective interaction enhances the PLL-STS of VSC$_k$ due to the reduced acceleration area.

The coefficients introduced in (18) serve as quantitative tools to assess the effects of static and dynamic interactions on the PLL-STS of individual converters. This is very useful for further understanding of the interaction behaviors between VSCs. Additionally, by comparing the absolute values of $\lambda_{\mathrm{d}k}$ and $\lambda_{\mathrm{s}k}$, it becomes possible to identify scenarios where the dynamic interaction can be ignored (when $|\lambda_{\mathrm{d}k}|$ is much smaller than $|\lambda_{\mathrm{s}k}|$), and those where it is essential must be considered (when there is little difference between $|\lambda_{\mathrm{d}k}|$ and $|\lambda_{\mathrm{s}k}|$, especially if $|\lambda_{\mathrm{d}k}|$ is larger than $|\lambda_{\mathrm{s}k}|$).

Note that the overall impact of transient interactions on the PLL-STS of VSC$_k$ can be represented by λ_k, which is the sum of $\lambda_{\mathrm{s}k}$ and $\lambda_{\mathrm{d}k}$.

D. Comparison With the Numerical Integration Method

Although the proposed method also needs numerical integration to obtain the system trajectory, it offers several key advantages over the numerical integration method:

1) *Faster transient synchronization stability evaluation:* The PLL-STS of the system can be evaluated faster by the proposed method. Unlike the numerical integration method, which solves the system trajectory over the entire transient process, our method uses numerical integration only for a brief period after the fault occurs. As illustrated in Fig. 3, the proposed method only requires numerical integration to obtain the system trajectory during the short period when δ_k moves from $\delta_{\mathrm{ke},0}$ to δ_{kd}. This approach significantly reduces the integration time required for transient stability evaluation, as validated in Section IV-A3.
2) *Identification of the dominant instability converters:* If the system is judged to be unstable, the dominant converters leading to instability can be identified by the proposed method, providing valuable guidance for emergency control. The corresponding RT-LAB hardware-in-the-loop experimental results are provided in Section IV-A3.
3) *Quantitative analysis of static and dynamic interaction:* The effects of static and dynamic interaction among converters on the PLL-STS of individual VSCs can be quantitatively analyzed based on the proposed method. This is very useful for further understanding the interaction behaviors between VSCs on the PLL-STS of individual converters. Detailed case analysis and experimental validation results are presented in Section IV-B.

IV. Verification

In this section, a three grid-tied VSCs system ($N=3$) is first built in the RT-LAB hardware-in-the-loop platform, as shown in Fig. 27 of Appendix C. On this basis, the PLL-STS assess-ment method and the interaction coefficients are validated in Sections IV-A and IV-B, respectively. Then, in Section IV-C, a detailed switching model of a nine grid-tied VSCs system ($N=9$) is built in PSCAD/EMTDC further to validate the effectiveness of the PLL-STS assessment method.

A. PLL-STS Assessment Method Verification by Three VSCs System

A three grid-tied VSCs system is built in the RT-LAB hardware-in-the-loop platform, with detailed parameters in Table VI of Appendix D. Two cases were considered, referred to as Case 1 and Case 2.

For Case 1 and Case 2, the $\mathbf{Z_F}$ is set at (0.0066 + 0.022j) pu and (0.006 + 0.02j) p.u/, respectively. The injected currents of the three VSCs during faults remained the same for both cases, with specific values provided in Table I. The power flow

TABLE I
INJECTED CURRENTS OF THREE VSCS DURING FAULTS IN BOTH CASES

Symbol	$I_{td\text{ref}1}$	$I_{tq\text{ref}1}$	$I_{td\text{ref}2}$	$I_{tq\text{ref}2}$	$I_{td\text{ref}3}$	$I_{tq\text{ref}3}$
Values	0.075	0.24	0.075	0.24	0.272	0.2

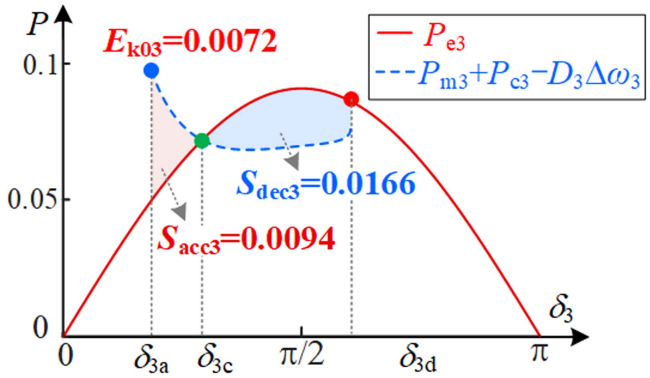

Fig. 5. Acceleration and deceleration area of VSC_3 for case 1.

TABLE II
ACCELERATION AND DECELERATION AREA OF CASE 1

VSC_k	S_{acck}	E_{k0k}	$S_{acck}+E_{k0k}$	S_{deck}	Meet (13)?
VSC_1	0.0069	0.0003	0.0072	0.0072	Yes
VSC_2	0.0018	0.0001	0.0019	0.0019	Yes
VSC_3	0.0094	0.0072	0.0166	0.0166	Yes

of prefault and postfault for Case 1 and Case 2 are provided in Tables VII and VIII of Appendix E, respectively.

Next, the PLL-STS of the three grid-tied VSCs system in Case 1 and Case 2 is analyzed using the PLL-STS assessment method proposed in Section III.

1) Transient Stability Analysis of Case 1: For Case 1, taking VSC_3 as an example, Fig. 5 presents the P_{e3}-δ_3 and $(P_{m3}+P_{c3}-D_3\Delta\omega_3)$ -δ_3 curves. Note that the amplitude of the pre-fault equivalent electromagnetic power between VSC_3 and grid $P_{e3,0}$ is much larger than the amplitude of the P_{e3}. Thus, the pre-fault $P_{e3,0}$-δ_3 curve is not presented in Fig. 5. In Fig. 5, S_{acc3} and S_{dec3} are the acceleration and deceleration areas of VSC_3, respectively. Applying the algorithm proposed in Fig. 4, the specific values of acceleration and deceleration areas for VSC_1, VSC_2, and VSC_3 can be obtained, listed in Table II. From II, the system satisfies the PLL-STS criterion (14), i.e., all three VSCs meet the criterion (13). Thus, the three grid-tied VSCs system must be transient stable for Case 1.

Fig. 6 depicts the experimental results of Case 1. From the experimental results, the system is stable in Case1. The experimental results agree with the theoretical analysis, verifying the validity of the PLL-STS evaluation method proposed in this paper.

2) Transient Stability Analysis of Case 2: For Case 2, the P_{e3}-δ_3 and $(P_{m3}+P_{c3}-D_3\Delta\omega_3)$-$\delta_3$ curves for VSC_3 are presented in Fig. 7. Specific values of acceleration and deceleration areas for three VSCs under Care 2 are detailed in Table III. From Table III, while VSC_1 and VSC_2 satisfy the stability criterion (13), VSC3 did not, as indicated by $S_{acc3}+E_{k03}>S_{dec3}$. Thus,

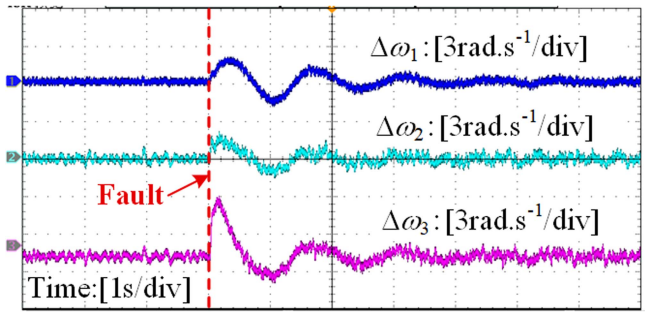

Fig. 6. Experimental results of case 1.

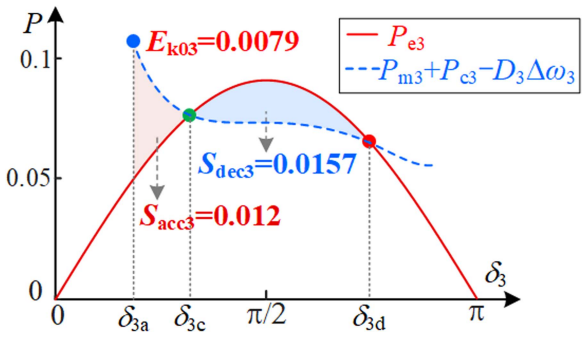

Fig. 7. Acceleration and deceleration area of VSC_3 for case 2.

TABLE III
ACCELERATION AND DECELERATION AREA OF CASE 2

VSC_k	S_{acck}	E_{k0k}	$S_{acck}+E_{k0k}$	S_{deck}	Meet (13)?
VSC_1	0.01	0.0003	0.0103	0.0103	Yes
VSC_2	0.0025	0.0001	0.0026	0.0026	Yes
VSC_3	0.012	0.0079	0.0199	0.0157	No

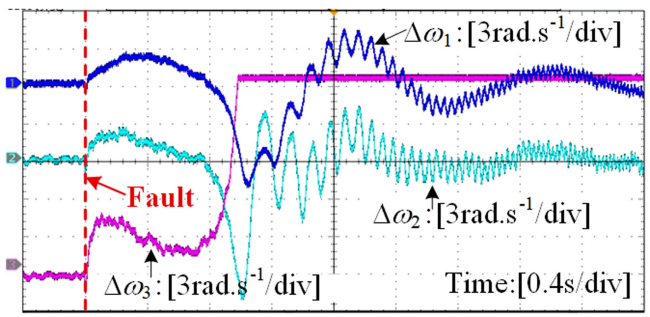

Fig. 8. Experimental results of case 2.

the system failed to meet the transient stability criterion (14), resulting in instability in Case 2.

The experimental results of Case 2 are presented in Fig. 8. Experimental results show that the system is unstable in Case 2, consistent with the theoretical analyses. Hence, the PLL-STS assessment method proposed in this article can efficiently analyze the PLL-STS of the MVSCs system.

3) Comparison With the Numerical Integration Method by Specific Cases: Compared to the numerical integration method,

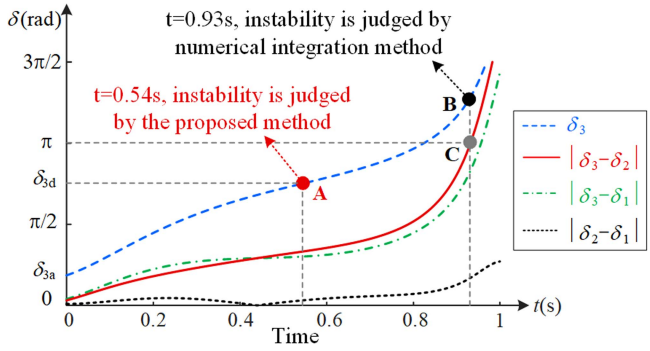

Fig. 9. Trajectory of the phase angle for VSC_3 and the absolute value of the phase angle difference for different converters in case 2.

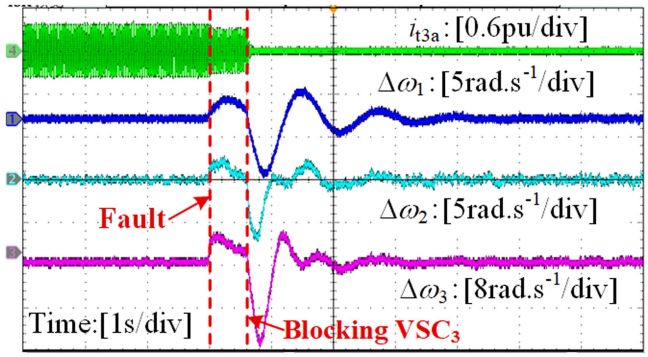

Fig. 10. Experimental results of blocking VSC_3 after fault occurrence 0.54 s.

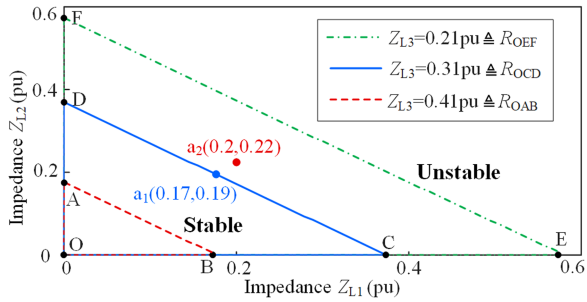

Fig. 11. Feasible regions of Z_{L1} and Z_{L2} to ensure transient stability.

our method offers advantages in faster stability evaluation, identification of dominant instability converters, and quantitative analysis of static and dynamic interactions. In this subsection, Case 2 is used as an example to illustrate the former two advantages of our method.

a) Faster stability evaluation: As shown in Fig. 7, in Case 2, the transient instability can be judged when δ_3 moves to δ_{3d} (0.54 s after the fault) based on our method. That is, for Case 2, using the proposed method, numerical integration is only required within 0.54 s after the fault.

For the numerical integration method, the criterion for evaluating the transient stability is whether the maximum phase angle difference between VSCs exceeds π, as shown in the following equation:

$$\max|\delta_i - \delta_j| \le \pi,\ (i,j = 1,\ldots,N, i \ne j)\,. \tag{19}$$

If the maximum phase angle difference is not greater than π, the MVSCs system is stable. Otherwise, the system is unstable.

Fig. 9 presents the trajectory of the phase angle for VSC_3 and the absolute value of the phase angle difference for different converters. From Fig. 9, when δ_3 moves to δ_{3e} (point B), $|\delta_3 - \delta_2|$ is equal to π and subsequently exceeds π. Thus, using the numerical integration method, the transient instability can be judged only when δ_3 moves to δ_{3e} (0.93 s after the fault). That is, for Case 2, using the numerical integration method, numerical integration is required within 0.93 s after the fault.

Overall, while both methods need numerical integration to obtain the system trajectory, our method requires a shorter integration time to evaluate the PLL-STS of the system. Thus, the PLL-STS of the MVSCs system can be evaluated faster by the method proposed in this paper than by the numerical integration method.

b) Dominant instability converters identification: From Table III, in Case2, only VSC_3 does not satisfy the stability criterion (13). Thus, VSC_3 is the dominant converter, causing the system transient instability under Case 2. Then, emergency controls, such as temporarily blocking VSC3 (by adjusting the reference current of VSC3 to 0), can prevent further deterioration of the stability of the entire system. The experimental results are shown in Fig. 10. From Fig. 10, the PLL-STS of the three grid-tied VSCs system can be ensured by blocking VSC3 after fault occurrence 0.54 s. Thus, the novel PLL-STS method proposed in this article is very helpful for the fault-ride-through of the system.

4) Analysis of the Effect of Impedance on Transient Stability: The system impedance is key for the transient stability of the whole system. Thus, the impact of the converter-side impedance $\mathbf{Z_{L}}_k$ ($k = 1, 2, 3$) and the grid-side impedances $\mathbf{Z_{Lg1}}$, $\mathbf{Z_{Lg2}}$, and $\mathbf{Z_F}$ on the PLL-STS of the MVSCs system is analyzed here. To simplify the analysis, we consider the phase angle of system impedance parameters to be the same in the following analyses and only explore the impact of impedance magnitude on the transient stability of the whole system. In the following, the current references of VSCs are selected to $I_{t\,dref1} = I_{t\,dref2} = 0.135$ p.u., $I_{t\,qref1} = I_{t\,qef2} = 0.24$ p.u., $I_{t\,dref3} = 0.2$ p.u., $I_{t\,qref3} = 0.2$ p.u., and $\mathbf{Z_F}$ is set to $(0.006 + 0.02\mathrm{j})$ p.u. Other parameters remain the same as those in Table VI.

a) Converter-side impedances: Fig. 11 presents the feasible regions R_{OEF}, R_{OCD}, and R_{OAB} of Z_{L1} and Z_{L2} to ensure transient stability of the MVSCs system with Z_{L3} selected to be 0.21, 0.31, and 0.41 p.u., respectively. The feasible region R_{OEF} in Fig. 11 implies that when Z_{L3} is equal to 0.21 p.u., the system is stable if the impedances Z_{L1} and Z_{L2} are in this region, else the system is unstable. From Fig. 11, increasing the impedance from the VSC_k to PCC (Z_{Lk}) deteriorates the transient stability of the MVSCs system.

Fig. 12(a) and (b) present the experimental results for two cases with parameters (Z_{L1}, Z_{L2}, Z_{L3}) selected to be $a_1(0.17, 0.19, 0.31)$ and $a_2(0.2, 0.22, 0.31)$, respectively. From Fig. 12(a), the system is stable when Z_{L1} and Z_{L2} are selected as 0.17

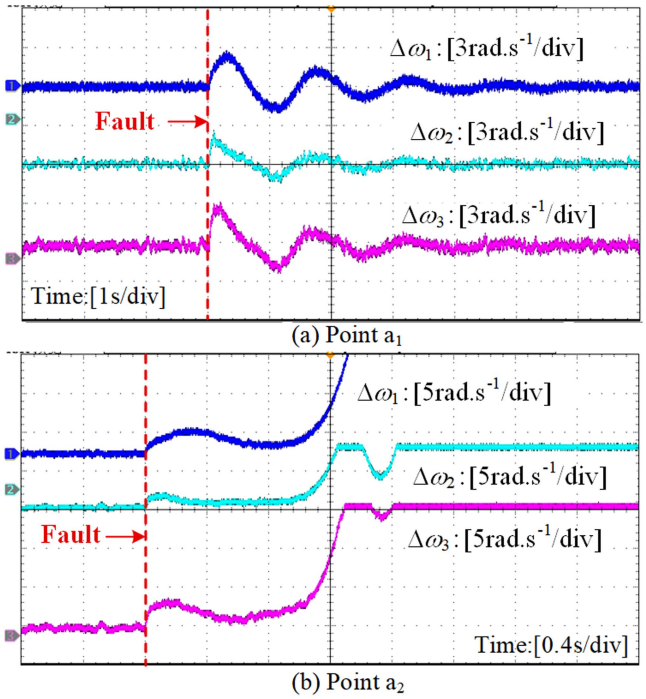

Fig. 12. Experimental results. (a) Point a_1. (b) Point a_2.

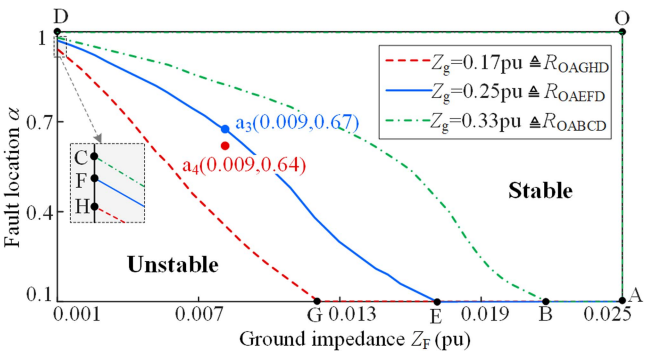

Fig. 13. Feasible regions of α and Z_F to ensure transient stability.

and 0.19 (point a_1), respectively. However, if Z_{L1} and Z_{L2} are increased to 0.2 and 0.22 (point a_2), respectively, the system is unstable, as shown in Fig. 12(b). The experiment results verify the theoretical analysis.

b) Grid-side impedances: The impedance from the PCC to the infinite bus $\boldsymbol{Z_g}$ and the fault location are critical factors. The expression for $\boldsymbol{Z_g}$ is given in (20), and α is defined in (21), indicating the distance of the fault from the PCC

$$\boldsymbol{Z_g} = \boldsymbol{Z_{Lg1}} + \boldsymbol{Z_{Lg2}} \tag{20}$$

$$\alpha = \boldsymbol{Z_{Lg1}}/(\boldsymbol{Z_{Lg1}} + \boldsymbol{Z_{Lg2}}). \tag{21}$$

Fig. 13 presents the feasible regions R_{OAGHD}, R_{OAEFD}, and R_{OABCD} of α and Z_F to ensure transient stability of the MVSCs system with Z_g selected to be 0.17, 0.25, and 0.33 p.u., respectively. From Fig. 13, the conclusions can be drawn as: 1) The greater the value of Z_g (indicating weaker grid strength) and the larger the value of Z_F (indicating more severe faults), the weaker the transient stability of the system. which is consistent with the existing literature [17], [18], [19], [20]. 2) The closer the fault location is to the PCC, the weaker the PLL-STS of the system, which will be verified in the following.

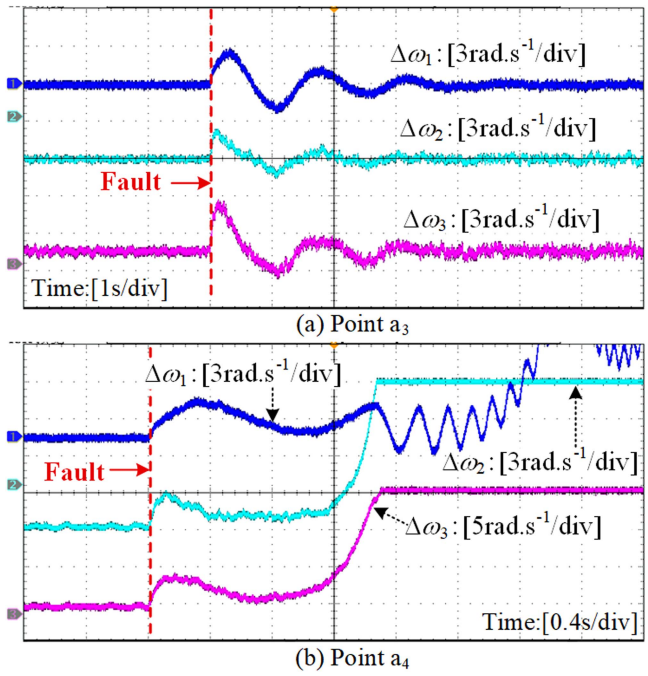

Fig. 14. Experimental results. (a) Point a_3. (b) Point a_4.

Fig. 14(a) and (b) present the experimental results for two cases with parameters (α, Z_F, Z_g) selected to be a_3(0.009, 0.67, 0.25) and a_4(0.009, 0.64, 0.25), respectively. As seen from Fig. 14(a), the system is stable with α selected to be 0.67. However, if the fault location is close to the PCC (α reduced to 0.64), the system is unstable, as shown in Fig. 14(b). The experiment results verify the theoretical analysis.

B. Interaction Coefficients Verification by Three-VSCs System

To verify the static and dynamic interaction coefficients proposed in this paper, the influence of the interaction between VSCs on the PLL-STS of VSC_3 is analyzed as an example. Besides the three grid-tied VSCs system, an additional single grid-tied VSC system is introduced as a comparative case to illustrate this influence, as depicted in Fig. 15.

Notably, all parameters of VSC_3 and VSC_{3e} in Fig. 15 are identical, except for the prefault active and reactive injected currents of VSC_{3e} ($I_{t\,dref,0}$ and $I_{t\,qref,0}$, respectively), determined by (22), ensuring an identical initial state for VSC_3 and VSC_{3e} [15]

$$\begin{cases} I_{tdref,0} = V_{t3e,0}G_{e3} - V_g G_{e3}\cos\delta_{3e,0} - V_g B_{e3}\sin\delta_{3e,0} \\ I_{tqref,0} = -V_{t3e,0}B_{e3} - V_g G_{e3}\sin\delta_{3e,0} + V_g B_{e3}\cos\delta_{3e,0} \end{cases} \tag{22}$$

where $V_{t3e,0}$ is the prefault POS_3 voltage; $G_{e3} = R_{e3}/({R_{e3}}^2 + {X_{e3}}^2)$, $B_{e3} = -X_{e3}/({R_{e3}}^2 + {X_{e3}}^2)$, $\boldsymbol{Z_{e3}} = R_{e3} + jX_{e3} = \boldsymbol{Z_{L3}} + \boldsymbol{Z_{Lg1}} + \boldsymbol{Z_{Lg2}}$.

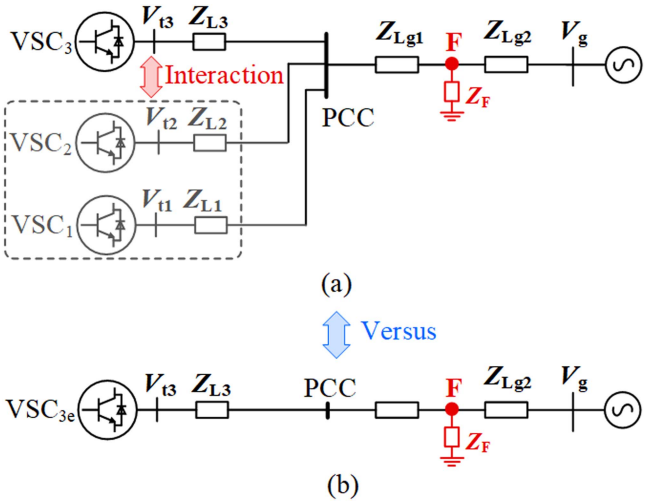

Fig. 15. (a) Three grid-tied VSCs system. (b) Single grid-tied VSC system is considered as a comparative case to demonstrate the influence of the interaction between VSCs on the PLL-STS of VSC_3.

TABLE IV
INJECTED CURRENTS OF THREE VSCS DURING FAULTS FOR CASE 3–CASE 5

Case	$I_{td\text{ref}1}$	$I_{tq\text{ref}1}$	$I_{td\text{ref}2}$	$I_{tq\text{ref}2}$	$I_{td\text{ref}3}$	$I_{tq\text{ref}3}$
Case 3	0.054	0.15	0.13	0.15	0.18	0.2
Case 4	0	0.225	0.03	0.18	0	0.3
Case 5	0.15	0.225	0.15	0.225	0.173	0.2

TABLE V
STATIC AND DYNAMIC INTERACTION COEFFICIENTS FOR CASE 3–CASE 5

Case	λ_{s3}	λ_{d3}	λ_3
Case 3	0.0016	−0.0041	−0.0025
Case 4	0.01	−0.027	−0.017
Case 5	0.056	0.02	0.076

Consider Case 3, Case 4, and Case 5, where the ground impedance is $(0.006 + 0.02j)$p.u., and the injected currents of three VSCs during faults are provided in Table IV. The static and dynamic interaction coefficients for Case 3–Case 5 are listed in Table V.

1) Case 3: The analysis revealed that the acceleration area $\Delta S_{cs3}(\lambda_{s3})$ corresponding to the static interaction P_{3cs} is 0.0016, indicating that static interaction deteriorates the PLL-STS of VSC_3. Conversely, the acceleration area $\Delta S_{cd3}(\lambda_{d3})$ corresponding to the dynamic interaction P_{3cd} is −0.0041, suggesting that dynamic interaction enhances the PLL-STS of VSC_3. Notably, the absolute values comparison $|\lambda_{s3}| < |\lambda_{d3}|$ implies that dynamic interaction has a greater influence on the PLL-STS of VSC_3 than static interactions. Hence, in this scenario, the transient interaction between VSCs, predominantly driven by dynamic interaction, enhances the transient stability of VSC_3.

Experimental results for three VSCs and single-VSC system in Case 3 are shown in Fig. 16(a) and (b), respectively.

As shown in Fig. 16(b), VSC_{3e} in the single grid-tied VSC system is unstable. However, VSC_3 in the three grid-tied VSCs system is stable due to the influence of the transient interaction between VSC_s, as depicted in Fig. 16(a). The experimental

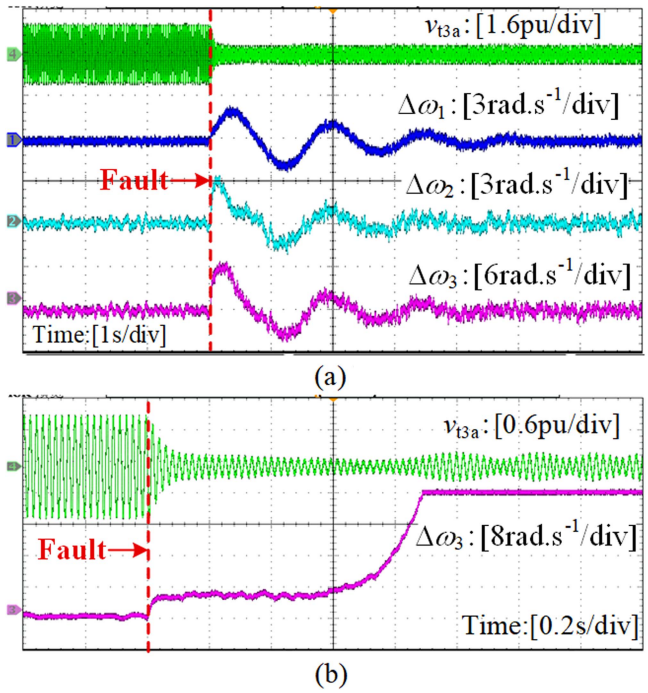

Fig. 16. Experimental results of case 3. (a) Three grid-tied VSCs system. (b) Single grid-tied VSC system. (a) With transient interaction. (b) Without Transient interaction.

results are in line with the theoretical analysis in Table V, verifying the validation of the interaction coefficients defined in this paper.

2) Case 4: Under this case, there are $\Delta S_{cs3}(\lambda_{s3}) > 0$ and $\Delta S_{cd3}(\lambda_{d3}) < 0$ holds, indicating that static interactions deteriorate, while dynamic interaction enhances the transient stability of VSC_3, respectively. By absolute values comparison, it is clear from Table V that there is $|\lambda_{s3}| < |\lambda_{d3}|$ holds, indicating that the effect of dynamic interaction on the PLL-STS of VSC_3 is greater than that of static interactions. Hence, the transient interaction between VSCs enhances the transient stability of VSC_3. The theoretical analysis is validated by experimental results in Fig. 17.

3) Case 5: Under this case, there are $\lambda_{s3} > 0$ and $\lambda_{d3} > 0$ holds, indicating that both static interactions and dynamic interactions deteriorate the PLL-STS of VSC_3. Hence, the transient interaction between VSCs deteriorates the transient stability of VSC_3. The theoretical analysis is validated by experimental results in Fig. 18.

From the analysis of Case 3–Case 5, three key conclusions can be drawn:

1) In specific scenarios, such as Case 3 and Case 4, the effects of static and dynamic interaction between VSC_s on the PLL-STS of a single converter may be opposite, and the dynamic interaction plays a more significant role. Thus, ignoring dynamic interaction may lead to incorrect conclusions.
2) It is improper to study the impact of dynamic interaction on the PLL-STS of individual VSCs by using its maximum value as proposed in [19]. For example, in Case 3, if

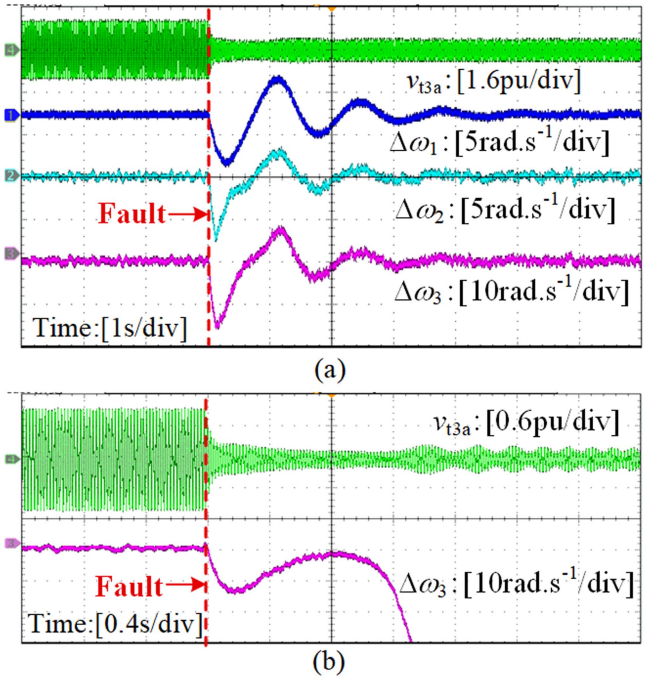

Fig. 17. Experimental results of case 4. (a) Three grid-tied VSCs system. (b) Single grid-tied VSC system. (a) With transient interaction. (b) Without Transient interaction.

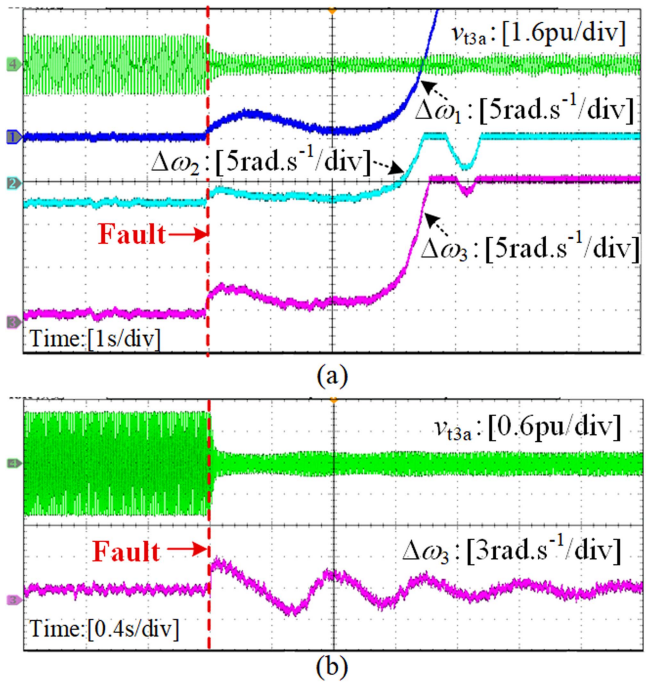

Fig. 18. Experimental results of case 5. (a) Three grid-tied VSCs system. (b) Single grid-tied VSC system. (a) With transient interaction. (b) Without Transient interaction.

the maximum value of the dynamic interaction is used to analyze its effect on the PLL-STS of VSC_3, the erroneous conclusion that the dynamic interaction worsens the PLL-STS of VSC_3 can be obtained.

3) The dynamic interactions may lead to different influences on the PLL-STS of individual VSCs in different scenarios.

C. Verification by the Grid-Tied Nine-VSCs System

To further verify the PLL-STS assessment method proposed in this article, a nine grid-tied VSCs system ($N = 9$) is built in PSCAD/EMTDC. The system structure is shown in Fig. 19. This system consists of nine VSCs, and each converter is connected to the PCC via a 10 kV/35 kV transformer and then to the infinity bus via a 35 kV/220 kV transformer. The total capacity of the nine-VSCs system is 48 MW. The rated capacity of VSC_1–VSC_6 and VSC_7–VSC_9 are 4 and 8 MW, respectively. The line lengths l_{Lk} of Z_{Lk}, the active/reactive current references of prefault ($I_{t\,dref k,0}/I_{t\,qref k,0}$) and fault-on ($I_{t\,dref k,1}/I_{t\,qref k,1}$) and the PLL control parameters for VSC_k are offered in Table IX of Appendix F. In Table IX, the line resistance and inductance per unit length are 1.05 mH/km and 0.1153 Ω/km, respectively [26]. In addition, Z_{Lg1} and Z_{Lg2} in Fig. 19 are both $(0.06 + 0.2j)$p.u.

We considered two different cases, Case 6 and Case 7. The ground impedance $\mathbf{Z_F}$ for Case 6 and Case 7 are $(0.0072 + 0.024j)$p.u. and $(0.006 + 0.02j)$p.u., respectively. The injected currents for each VSC during faults are listed in Table IX. The power flow of prefault and postfault for Case 6 and Case 7 are provided in Tables X and XI of Appendix F, respectively. The detailed switching model simulation results for Case 6 and Case 7 are shown in Figs. 20 and 21, respectively.

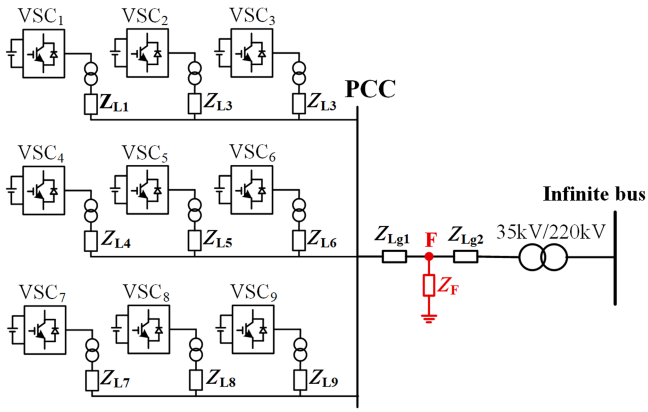

Fig. 19. Topology of the nine grid-tied VSCs system.

Applying the algorithm proposed in Fig. 4, the specific values of acceleration and deceleration areas of each VSC can be calculated, which are listed in Tables XII and XIII in Appendix F, respectively.

For Case 6, all VSCs satisfy the stability criterion (13). Thus, the nine grid-tied VSCs system must be transient stable for Case 6. However, in Case 7, while VSC_1∼VSC_8 satisfies criterion (13), VSC_9 is not satisfied, as shown in Table XIII. Hence, the system is transient instability under Case 7. The theoretical analysis results are consistent with the results derived from the simulations, confirming the effectiveness of the proposed transient stability assessment method.

For Case 7, VSC_9 was identified as not satisfying the stability criterion (13). Therefore, VSC_9 is the dominant converter, causing the system transient instability. To validate this, VSC_9

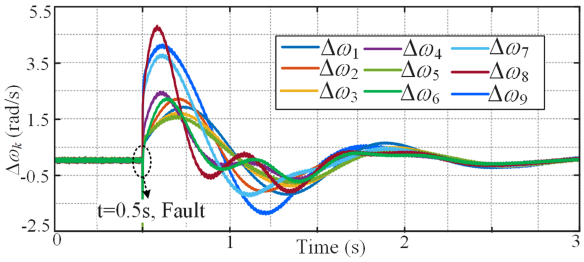

Fig. 20. Simulation results of the nine grid-tied VSCs system for case 6.

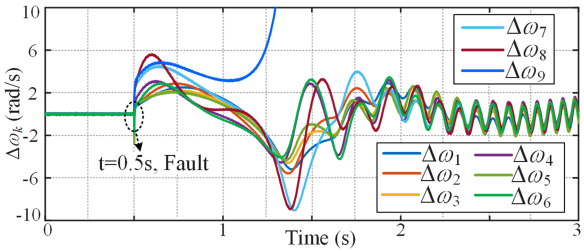

Fig. 21. Simulation results of the nine grid-tied VSCs system for case 7.

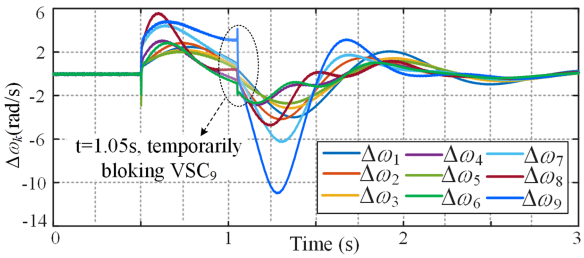

Fig. 22. Simulation results of VSC_9 being isolated at 1.05 s under case 7.

is blocked at $t = 1.05$ s under Case 7. The simulation results are shown in Fig. 22.

From Fig. 22, after VSC_9 is blocked, VSC_1–VSC_8 can all remain stable. This indicates that VSC_9 is the dominant converter causing instability in the grid-tied nine-VSCs system under Case 7. Thus, when the system experiences transient instability, the PLL-STS assessment method proposed in this paper can effectively identify the dominant transient instability when instability occurs, which is very helpful for the fault-ride-through of the MVSCs system.

V. Discussion

In this section, the robustness of the proposed method against parameter uncertainties is discussed in Section V-A. Then, the applicability of the proposed method considering voltage-dependent current injection is discussed in Section V-B.

A. Robustness of the Proposed Method Against Parameter Uncertainties

The method proposed in this article relies on parameter knowledge. Accurately obtaining the system parameters, especially the grounding impedance, is very challenging in a real system, and these parameters always have some degree of uncertainty. To address this concern and illustrate the robustness of our method against parameter uncertainties, we have conducted an analysis using the grounding reactance X_F as an example in this article. The system parameters are listed in Table VI, with R_F set to 0.006 p.u., and the injected current of the three VSCs during faults is consistent with Table I.

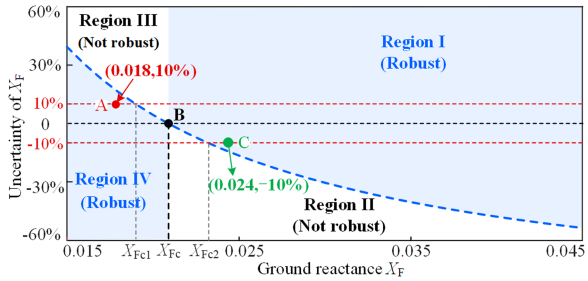

Fig. 23. Robustness of the method under different uncertainties when X_F is increased from 0.015 to 0.045 p.u.

Fig. 23 gives the robustness of the method under different uncertainties when X_F is increased from 0.015 to 0.045 p.u. The detailed explanation of Fig. 23 is presented as follows:

1) *Critical grounding reactance:* According to the electromagnetic transient simulation results, the system is stable when X_F is not less than X_{Fc}(0.021 p.u.). Otherwise, the system is transient instability. Hence, X_{Fc} (point B) is the critical grounding reactance that maintains the system stable.
2) *Robustness in Region IV:* When X_F is less than X_{Fc}, if the uncertainties of X_F lie within Region IV, the proposed method yields the same transient instability result as the simulation results. That is, the method is robust within the uncertainties of Region IV.
3) *Robustness in Region I:* When X_F is greater than X_{Fc}, if the uncertainties of X_F lie within Region I, the method proposed in this paper yields the same transient stability result as the simulation results. That is, the method is robust within the uncertainties of Region I.
4) *Non-Robust Regions II and III:* If the uncertainties of X_F fall within regions II or III, the proposed calculation method cannot yield consistent results with the simulation results, indicating a lack of robustness in these regions.

As shown in Fig. 23, the proposed method demonstrates good robustness to parameter uncertainty in most scenarios. Specifically, when X_F is within the intervals [0.015, X_{Fc1}] and [X_{Fc2}, 0.045], the calculation method proposed in this article is robust under $\pm 10\%$ of parameter uncertainty. Only when X_F is very close to X_{Fc}, the calculation method will be very sensitive to parameter uncertainty. In this scenario, how to improve the robustness of the proposed method in this article against parameter uncertainty will be the next focus of our work.

B. Applicability of the Proposed Method Considering Voltage-Dependent Current Injection

To simplify the analysis, fixed active and reactive injected currents are considered in the main contents of the article.

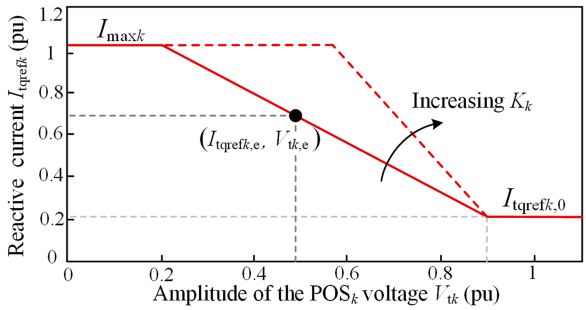

Fig. 24. VDCI defined by the grid code of VSC$_k$.

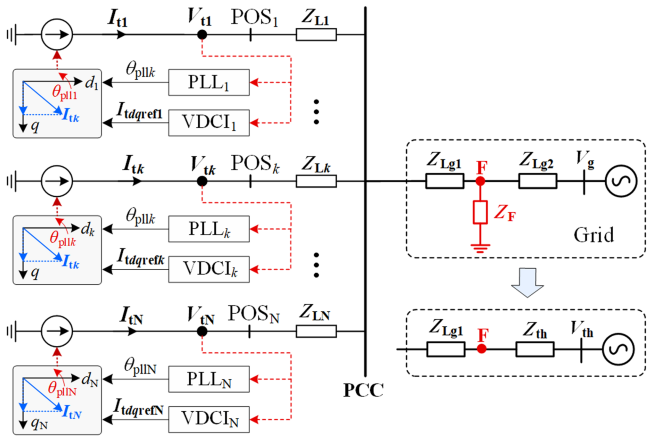

Fig. 25. Equivalent circuit of the MVSCs system considering VDCI dynamics.

However, according to the grid code, the injected reactive current by VSC during faults should be dynamically adjusted depending on the voltage variation, which is referred to as voltage-dependent current injection (VDCI) in the following. This section develops a mathematical model of the MVSCs system considering VDCI dynamics and discusses the applicability of the proposed method under these conditions.

Using VSC$_k$ as an example, the VDCI defined by grid code is introduced. During a grid fault, if the voltage dip at POS of VSC$_k$ exceeds 10%, VSC$_k$ is required to inject reactive current proportional for voltage support [27], [28], as shown in Fig. 24, where $I_{\mathrm{t}qrefk,0}$ is the prefault reactive current injection. In Fig. 24, K_{k} is the reactive current injection proportional coefficient K-factor in the range of 0–10 [29], [30], and the solid dot represents a possible steady-state operating point during faults. Note that $I_{\mathrm{t}qrefk}$ will not reach the maximum injected current $I_{\mathrm{max}k}$ allowed by VSC$_k$ when K_k is small. This section focuses on the PLL-STS of the system under these conditions.

There are no specific grid code requirements for active power injection $I_{\mathrm{td}refk}$ and the remaining converter power capacity is typically utilized. Thus, considering VDCI dynamics, $I_{\mathrm{td}refk}$ and $I_{\mathrm{tq}refk}$ during faults can be expressed as follows:

$$\begin{cases} I_{\mathrm{tq}refk} = I_{\mathrm{tq}refk,0} + K_k\left(0.9 - V_{\mathrm{t}k}\right) \\ I_{\mathrm{td}refk} = \sqrt{{I_{\mathrm{max}\,k}}^2 - {I_{\mathrm{tq}refk}}^2}. \end{cases} \tag{23}$$

Considering VDCI dynamics, the equivalent circuit of the MVSCs system is presented in Fig. 25.

Combining (23) and Fig. 25, the POS voltage of VSC$_k$ can be expressed as follows:

$$\boldsymbol{V_{\mathrm{t}k}} = K_{\mathrm{g}}V_{\mathrm{g}}e^{j\left(\theta_{\mathrm{g}}+\varphi_{\mathrm{g}}\right)} + Z_k I_{\mathrm{max}k}e^{j\left(\theta_{\mathrm{pll}k}-\theta_{Ik}+\varphi_k\right)} + Z_{\mathrm{e}}\sum_{j=1,j\neq k}^{N} I_{\mathrm{max}j}e^{j\left(\theta_{\mathrm{pll}j}-\theta_{Ij}+\varphi_{\mathrm{e}}\right)}. \tag{24}$$

The expression for θ_{Ik} in (24) is given in the following:

$$\theta_{Ik} = \arctan\left(\frac{I_{\mathrm{tq}refk,0} + K_k\left(0.9 - V_{\mathrm{t}k}\right)}{\sqrt{{I_{\mathrm{max}\,k}}^2 - \left(I_{\mathrm{tq}refk,0} + K_k\left(0.9 - V_{\mathrm{t}k}\right)\right)^2}}\right). \tag{25}$$

Transforming $\boldsymbol{V_{\mathrm{t}k}}$ to the dq_k coordinate system, the d-axis and q-axis components of POS$_k$ voltage can be obtained as follows:

$$\begin{cases} V_{tdk} = K_{\mathrm{g}}V_{\mathrm{g}}\cos\left(\theta_{\mathrm{pll}k} - \theta_{\mathrm{g}} - \varphi_{\mathrm{g}}\right) + Z_k I_{\mathrm{max}\,k}\cos\left(\theta_{Ik} - \varphi_k\right) \\ \qquad + Z_{\mathrm{e}}\sum_{j=1,j\neq k}^{N} I_{\mathrm{max}\,j}\cos\left(\delta_{kj} + \theta_{Ij} - \varphi_{\mathrm{e}}\right) \\ V_{tqk} = K_{\mathrm{g}}V_{\mathrm{g}}\sin\left(\theta_{\mathrm{pll}k} - \theta_{\mathrm{g}} - \varphi_{\mathrm{g}}\right) + Z_k I_{\mathrm{max}\,k}\sin\left(\theta_{Ik} - \varphi_k\right) \\ \qquad + Z_{\mathrm{e}}\sum_{j=1,j\neq k}^{N} I_{\mathrm{max}\,j}\sin\left(\delta_{kj} + \theta_{Ij} - \varphi_{\mathrm{e}}\right). \end{cases} \tag{26}$$

The magnitude of $V_{\mathrm{t}k}$ can be calculated as follows:

$$V_{tk} = \sqrt{{V_{tdk}}^2 + {V_{tqk}}^2}. \tag{27}$$

Then, combining the dynamic equations of PLL$_k$ and (25)–(27), we can obtain the nonlinear model for the MVSCs system considering VDCI dynamics, as formulated in the following:

$$\begin{cases} \dot{\delta}_k = \omega_{\mathrm{pll}k} - \omega_0 \triangleq \Delta\omega_k \\ J_k\Delta\dot{\omega}_k = \underbrace{\left(P_{\mathrm{m}k} + P_{\mathrm{I}k}\right)}_{P_{\mathrm{m}k\_\mathrm{I}}} - P_{\mathrm{e}k} - D_k\Delta\omega_k \\ \quad + \underbrace{\left(P_{\mathrm{c}k} + P_{\mathrm{cI}k}\right)}_{P_{\mathrm{c}k\_\mathrm{I}}} \\ \Delta\omega_k\left(t_0{}^+\right) = -k_{\mathrm{p}k}V_{tqk}\left(t_0{}^+\right). \end{cases} , k = 1, \ldots, N \tag{28}$$

The meaning and specific expressions of J_k, D_k, $P_{\mathrm{m}k}$, $P_{\mathrm{e}k}$, $P_{\mathrm{c}k}$, and $V_{\mathrm{t}qk}(\mathrm{t_0}^+)$ in (28) are consistent with not considering the VDCI dynamic, as shown in (9). Compared without the VDCI dynamic, the system model considering the VDCI dynamic has additional $P_{\mathrm{I}k}$ and $P_{\mathrm{cI}k}$. $P_{\mathrm{I}k}$ reflects the effect of the interaction between the VDCI dynamic of VSC$_k$ and the grid on the transient stability of VSC$_k$; $P_{\mathrm{cI}k}$ reflects the effect of VDCI dynamics of VSCs except for VSC$_k$ on the transient stability of VSC$_k$. The expressions for $P_{\mathrm{I}k}$ and $P_{\mathrm{cI}k}$ are given in (29)

$$\begin{cases} P_{\mathrm{I}k} = -k_{\mathrm{p}k}Z_k I_{\mathrm{tref}k}\cos\left(\theta_{Ik} - \varphi_k\right)\theta_{Ij}{}'/k_{\mathrm{i}k} \\ P_{\mathrm{cI}k} = -Z_{\mathrm{e}}\sum_{j=1,j\neq k}^{N} k_{\mathrm{p}k}I_{\mathrm{tref}j}\cos\left(\delta_{kj} + \theta_{Ij} - \varphi_{\mathrm{e}}\right)\theta_{Ij}{}'/k_{\mathrm{i}k}. \end{cases} \tag{29}$$

A comparison of (28) and (8) indicates that the model of the MVSCs system considering the VDCI dynamic has a similar form as not considering the VDCI dynamic. Consequently, even if the VDCI dynamic is considered, the acceleration area and deceleration area of VSC$_k$ during faults can still be calculated using the algorithm proposed in Fig. 4 and the PLL-STS of the system can be assessed using the criterion (13). The sole difference lies in the fact that considering the VDCI dynamic, the equivalent mechanical power of VSC$_k$ becomes $P_{\mathrm{m}k}+P_{\mathrm{I}k}$, and the equivalent electromagnetic interactive power between VSC$_k$ and other VSCs becomes $P_{\mathrm{c}k}+P_{\mathrm{cI}k}$. Therefore, the proposed method can be extended to PLL-STS analysis of the MVSCs system considering VDCI dynamic, which is a focus of our future work.

VI. Conclusion

This article presents a comprehensive investigation into the PLL-STS of the MVSCs systems, focusing on transient stability evaluation and transient interaction analysis. The main findings of this study can be summarized as follows.

1) A novel PLL-STS assessment method for the MVSCs system has been developed. The method can accurately evaluate the PLL-STS of the system since the acceleration and deceleration areas of VSCs are accurately determined by combining the EAC and numerical integration methods. Moreover, the method can also be applied to analyze the PLL-STS of grid-tied N-converter systems.
2) In the MVSCs system, instability in any converter can cascade to others, posing a significant threat to overall system transient stability. Using the PLL-STS assessment algorithm proposed in this article, the dominant converters leading to transient instability can be effectively identified. Then, emergency controls, such as temporarily blocking these converters, can prevent the further deterioration of overall system transient stability.
3) Previous works have often ignored dynamic interaction or oversimplified it by scaling the influence of dynamic interaction item to its maximum value when evaluating its influence on the PLL-STS of individual converters. However, our theoretical analyses in this article emphasize the importance of considering the variability inherent in dynamic interaction. This is because, in specific scenarios, ignoring or simplifying dynamic interaction may lead to misleading conclusions.

In this article, we have focused on theoretical analysis and introduced a novel method for PLL-STS assessment of the MVSCs system. For future work, we will consider the practical implementation aspects of the proposed strategy in a real multiconverter scenario.

Appendix A

The relationship between the $\theta_{\mathrm{pll}k}$ and the voltage vector $\boldsymbol{V_{\mathrm{t}k}}$ is shown in Fig. 26.

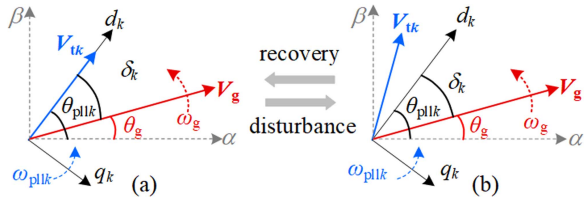

Fig. 26. The relationship between the $\theta_{\mathrm{pll}k}$ and the voltage vector $V_{\mathrm{t}k}$. (a) Steady state. (b) Transient state.

Appendix B

For the grid-tied multiple synchronous generators (SGs) system, the synchronous dynamic equation of the system is presented as follows:

$$\begin{cases}\dot{\delta}_{k\_\mathrm{SG}}=\Delta\omega_{k\_\mathrm{SG}}\\ J_{k\_\mathrm{SG}}\Delta\dot{\omega}_{k\_\mathrm{SG}}=P_{\mathrm{m}k\_\mathrm{SG}}-P_{\mathrm{e}k\_\mathrm{SG}}-D_{k\_\mathrm{SG}}\Delta\omega_{k\_\mathrm{SG}}+P_{\mathrm{c}k\_\mathrm{SG}}\end{cases} \tag{B1}$$

where $k=1,\ \ldots, N$; $\delta_{k\_\mathrm{SG}}=\theta_{\mathrm{SG}k}-\theta_{\mathrm{g}}$, and $\Delta\omega_{k\_\mathrm{SG}}=\omega_{\mathrm{SG}k}-\omega_{\mathrm{g}}$, denote the phase angle difference and angular frequency difference between SG$_k$ and infinite bus voltage, respectively; $P_{\mathrm{e}k\_\mathrm{SG}}$ is the electromagnetic power between SG$_k$ and grid; $P_{\mathrm{c}k\_\mathrm{SG}}$ is the interactive electromagnetic power between SG$_k$ and other SGs, reflecting the impacts of the transient interaction between SG$_s$ on the SG$_k$. The expressions for J_{k_SG}, D_{k_SG}, $P_{\mathrm{m}k\_\mathrm{SG}}$, $P_{\mathrm{e}k\_\mathrm{SG}}$, and $P_{\mathrm{c}k\_\mathrm{SG}}$ are detailed in (B2), where $\delta_{kj\_\mathrm{SG}}=\theta_{\mathrm{SG}k}-\theta_{\mathrm{SG}j}$, denotes the phase angle difference between SG$_k$ and SG$_j$

$$\begin{cases}J_{k\_\mathrm{SG}}=J_k, D_{k\_\mathrm{SG}}=D_k\\ P_{\mathrm{m}k\_SG}=P_{\mathrm{m}k}\\ P_{\mathrm{e}k\_SG}=K_{kg}V_{\mathrm{t}k}V_{\mathrm{g}}\sin\left(\delta_{k\_\mathrm{SG}}-\varphi_{kg}\right)+{V_{\mathrm{t}k}}^2G_{kk}\\ P_{\mathrm{c}k\_\mathrm{SG}}=\sum_{j=1,j\neq i}^{\mathrm{N}}V_{\mathrm{t}k}V_{\mathrm{t}j}K_{kj}sin\left(\delta_{kj\_\mathrm{SG}}-\varphi_{kj}\right)\end{cases} \tag{B2}$$

where $K_{kg}=1/\{{G_{kg}}^2+{B_{kg}}^2\}1/2$, $\varphi_{kg}=-\arctan\left(G_{kg}/B_{kg}\right)$; G_{kg} and B_{kg} are the transfer conductance and susceptance from node k to the infinite bus, respectively; Node k is the output voltage node of SG$_k$; $K_{kj}=1/\{{G_{kj}}^2+{B_{kj}}^2\}1/2$, $\varphi_{kj}=-\arctan\left(G_{kj}/B_{kj}\right)$; G_{kj} and B_{kj} are the transfer conductance and susceptance from node k to j, respectively; $V_{\mathrm{t}k}$ is the amplitude of the voltage at node k, G_{kk} is the self-conductance of node k.

Appendix C

The RT-LAB hardware-in-the-loop platform is as follows.

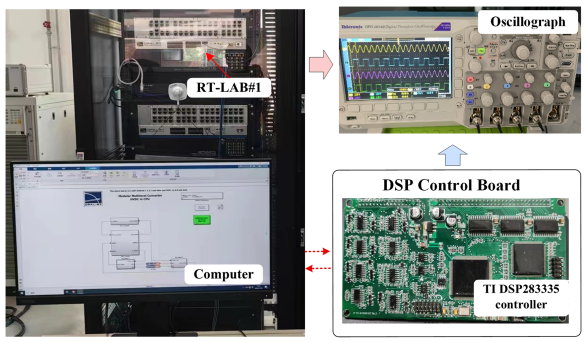

Fig. 27. RT-LAB hardware-in-the-loop platform.

APPENDIX D

TABLE VI
SYSTEM PARAMETERS OF THE THREE GRID-TIED VSCS

System	Parameter name	Value
Base values	Base value of Power	5 MW
	Base value of AC voltage	10 kV
	Base value of frequency	50 Hz
	Capacity of VSC_1/VSC_2/VSC_3	1.5/1.5/2 MW
Hardware parameter	Switching frequency	10 kHz
	LC filter of VSC_1, VSC_2, and VSC_3 are same	0.12/0.04 pu
	X_{Lg1}/R_{Lg1}	0.2/0.06 pu
	X_{Lg2}/R_{Lg2}	0.2/0.06 pu
	X_{L1}/R_{L1}	0.2/0.06 pu
	X_{L2}/R_{L2}	0.3/0.09 pu
	X_{L3}/R_{L3}	0.5/0.15 pu
	$I_{tdref1,0}/I_{tqref1,0}$	0.3/0.06 pu
	$I_{tdref2,0}/I_{tqref2,0}$	0.3/0.06 pu
	$I_{tdref3,0}/I_{tqref3,0}$	0.4/0.08 pu
	$V_{g,0}$	1 pu
Control parameter	PLL parameters of VSC_1 k_{p1}/k_{i1}	20 / 250
	PLL parameters of VSC_2 k_{p2}/k_{i2}	40/ 1000
	PLL parameters of VSC_3 k_{p3}/k_{i3}	30/500
	Bandwidth of PLL_1	4.9 Hz
	Bandwidth of PLL_2	9.86 Hz
	Bandwidth of PLL_3	7.15 Hz
	Current control of VSC_1, VSC_2, and VSC_3 are same	2/200
	Bandwidth of current control	847.3 Hz

APPENDIX E

TABLE VII
POWER FLOW INFORMATION OF PREFAULT FOR CASE 1 AND CASE 2

Bus Number	V(pu)	P(MW)	Q(MW)
1	1.07∠0.46	1.6	0.3
2	1.08∠0.49	1.62	0.3
3	1.12∠0.59	2.2	0.42
4	1.045∠0.41	/	/

Note: *Bus k is the VSC_k (k=1, …, 3) output voltage node; Bus 4 is the PCC node.

TABLE VIII
POWER FLOW INFORMATION OF POSTFAULT FOR CASE 1 AND CASE 2

Bus number	Case 1			Case 2		
	V(pu)	P (MW)	Q (MW)	V	P (MW)	Q (MW)
1	0.26∠0.86	0.1	0.3	0.23∠1.04	0.09	0.28
2	0.28∠0.86	0.11	0.33	0.26∠1.04	0.1	0.3
3	0.3∠1.39	0.42	0.3	0.28∠1.65	0.38	0.28
4	0.2∠0.85	/	/	0.18∠1.03	/	/

APPENDIX F

TABLE IX
LINE LENGTHS L_{Lk} (KM) OF $\mathbf{Z_{Lk}}$, THE ACTIVE/REACTIVE CURRENT REFERENCES OF PREFAULT AND FAULT-ON, AND THE PLL CONTROL PARAMETERS FOR VSC_k

VSC_k	l_{Lk}	$I_{tdrefk,0}$	$I_{tqrefk,0}$	$I_{tdrefk,1}$	$I_{tqrefk,1}$	k_{pk}	k_{ik}	f_{bwk}
VSC_1	12	0.083	0	0.033	0.067	20	250	4.9
VSC_2	18	0.083	0.033	0.033	0.05	20	375	5.65
VSC_3	8	0.083	0.033	0	0.083	30	250	6
VSC_4	25	0.083	0.033	0.033	0.083	40	1000	9.86
VSC_5	20	0.083	0.0167	0	0.083	30	1000	9
VSC_6	30	0.083	0.0167	0.167	0.083	40	250	7.3
VSC_7	40	0.167	0.082	0.117	0.033	30	500	7.15
VSC_8	46	0.167	0.083	0.1	0.033	30	1000	9
VSC_9	50	0.167	0.03273	0.133	0.05	30	400	6.73

Note: * f_{bwk} denotes the bandwidth of PLL_k (Hz).

TABLE X
POWER FLOW INFORMATION OF PREFAULT FOR CASE 6 AND CASE 7

Bus Number	V(pu)	P(MW)	Q(MW)
1	1.1∠0.38	4.56	0.054
2	1.12∠0.39	4.6	1.78
3	1.11∠0.38	4.57	1.77
4	1.13∠0.4	4.6	1.8
5	1.12∠0.39	4.6	0.86
6	1.12∠0.4	4.6	0.87
7	1.12∠0.45	9.6	4.7
8	1.16∠0.46	9.7	4.8
9	1.18∠0.48	9.5	1.8
10	1.14∠0.37	/	/

Note:*Bus k is the VSC_k (k=1, …, 9) output voltage node; Bus 10 is the PCC node.

TABLE XI
POWER FLOW INFORMATION OF POST-FAULT FOR CASE 6 AND CASE 7

Bus number	Case 6			Case 7		
	V(pu)	P (MW)	Q (MW)	V	P (MW)	Q (MW)
1	0.21∠0.79	0.34	0.67	0.173∠1	0.28	0.54
2	0.21∠0.8	0.34	0.5	0.174∠1.03	0.28	0.42
3	0.2∠0.76	0	0.5	0.172∠0.97	0	0.67
4	0.24∠0.79	0.37	0.93	0.194∠1.01	0.3	0.77
5	0.23∠0.74	0	0.88	0.184∠0.95	0	0.73
6	0.24∠0.76	0.2	0.95	0.2∠0.97	0.16	0.79
7	0.23∠1.12	1.27	0.36	0.184∠1.43	1.03	0.29
8	0.23∠1.1	1.1	0.4	0.188∠1.41	0.9	0.29
9	0.24∠1.26	1.56	0.58	0.2∠1.62	1.26	0.47
10	0.2∠0.78	/	/	0.174∠0.99	/	/

TABLE XII
ACCELERATION AND DECELERATION AREA OF CASE 6

VSC_k	S_{acck}	E_{k0k}	S_{acck}+E_{k0k}	S_{deck}	Meet (13)?
VSC_1	0.0064	0.006	0.007	0.007	Yes
VSC_2	0.0055	0.0005	0.006	0.006	Yes
VSC_3	0.0043	0.0012	0.0055	0.0055	Yes
VSC_4	0.0022	0.0006	0.0028	0.0028	Yes
VSC_5	0.0022	0.0001	0.0023	0.0023	Yes
VSC_6	0.0032	0.0012	0.0044	0.0044	Yes
VSC_7	0.008	0.006	0.014	0.014	Yes
VSC_8	0.0086	0.0024	0.011	0.011	Yes
VSC_9	0.01	0.01	0.02	0.02	Yes

TABLE XIII
ACCELERATION AND DECELERATION AREA OF CASE 7

VSC_k	S_{acck}	E_{k0k}	S_{acck}+ E_{k0k}	S_{deck}	Meet (13)?
VSC_1	0.0116	0.001	0.0126	0.0126	Yes
VSC_2	0.0102	0.0008	0.011	0.011	Yes
VSC_3	0.0082	0.0018	0.01	0.01	Yes
VSC_4	0.0038	0.0009	0.0047	0.0047	Yes
VSC_5	0.004	0.0002	0.0042	0.0042	Yes
VSC_6	0.0063	0.002	0.0083	0.0083	Yes
VSC_7	0.013	0.0064	0.0194	0.0194	Yes
VSC_8	0.0125	0.003	0.0155	0.0155	Yes
VSC_9	0.0162	0.0121	0.0283	0.0198	No

REFERENCES

[1] Y. Gu and T. C. Green, "Power system stability with a high penetration of inverter-based resources," *Proc. IEEE*, vol. 111, no. 7, pp. 832–853, Jul. 2023.

[2] M. G. Taul, X. Wang, P. Davari, and F. Blaabjerg, "Reduced-order and aggregated modeling of large-signal synchronization stability for multi-converter systems," *IEEE J. Emerg. Sel. Topics Power Electron.*, vol. 9, no. 3, pp. 3150–3165, Jun. 2021.

[3] Y. Li, Y. Tang, Y. Lu, F. Hua, and Z. Du, "Synchronization stability of grid-connected VSC with limits of PLL," *IEEE Trans. Power Syst.*, vol. 38, no. 4, pp. 3965–3976, Jul. 2023.
[4] M. G. Taul, X. Wang, P. Davari, and F. Blaabjerg, "An overview of assessment methods for synchronization stability of grid-connected converters under severe symmetrical grid faults," *IEEE Trans. Power Electron.*, vol. 34, no. 10, pp. 9655–9670, Oct. 2019.
[5] X. He, H. Geng, J. Xi, and J. M. Guerrero, "Resynchronization analysis and improvement of grid-connected VSCs during grid faults," *IEEE J. Emerg. Sel. Topics Power Electron.*, vol. 9, no. 1, pp. 438–450, Feb. 2021.
[6] H. Wu and X. Wang, "Design-oriented transient stability analysis of PLL-synchronized voltage-source converters," *IEEE Trans. Power Electron.*, vol. 35, no. 4, pp. 3573–3589, Apr. 2020.
[7] Q. Hu, L. Fu, F. Ma, and F. Ji, "Large signal synchronizing instability of PLL-based VSC connected to weak AC grid," *IEEE Trans. Power Syst.*, vol. 34, no. 4, pp. 3220–3229, Jul. 2019.
[8] X. Li et al., "The largest estimated domain of attraction and its applications for transient stability analysis of PLL synchronization in weak-grid-connected VSCs," *IEEE Trans. Power Syst.*, vol. 38, no. 5, pp. 4107–4121, Sep. 2023.
[9] Y. Ma, D. Zhu, Z. Zhang, X. Zou, J. Hu, and Y. Kang, "Modeling and transient stability analysis for type-3 wind turbines using singular perturbation and lyapunov methods," *IEEE Trans. Ind. Electron.*, vol. 70, no. 8, pp. 8075–8086, Aug. 2023.
[10] Y. Ma et al., "Reduced-order modeling and transient stability analysis of grid-connected VSC in DC-link voltage control timescale," *IEEE J. Emerg. Sel. Topics Power Electron.*, vol. 12, no. 3, pp. 2981–2993, Jun. 2024.
[11] Z. Zou, B. D. Besheli, R. Rosso, M. Liserre, and X. Wang, "Interactions between two phase-locked loop synchronized grid converters," *IEEE Trans. Ind. Appl.*, vol. 57, no. 4, pp. 3935–3947, Jul./Aug. 2021.
[12] R. Rosso, M. Andresen, S. Engelken, and M. Liserre, "Analysis of the interaction among power converters through their synchronization mechanism," *IEEE Trans. Power Electron.*, vol. 34, no. 12, pp. 12321–12332, Dec. 2019.
[13] S. Chen, J. Yao, Y. Liu, J. Pei, S. Huang, and Z. Chen, "Coupling mechanism analysis and transient stability assessment for multi-paralleled wind farms during LVRT," *IEEE Trans. Sustain. Energy*, vol. 12, no. 4, pp. 2132–2145, Oct. 2021.
[14] X. He and H. Geng, "Synchronization stability analysis and enhancement of grid-tied multi-converter systems," in *Proc. IEEE Ind. Appl. Soc. Annu. Meeting*, 2020, pp. 1–8.
[15] X. He and H. Geng, "PLL synchronization stability of grid-connected multi-converter systems," *IEEE Trans. Ind. Appl.*, vol. 58, no. 1, pp. 830–842, Jan./Feb. 2022.
[16] U. Buragohain and N. Senroy, "Reduced order DFIG models for PLL-based grid synchronization stability assessment," *IEEE Trans. Power Syst.*, vol. 38, no. 5, pp. 4628–4639, Sep. 2023.
[17] X. Yi et al., "Transient synchronization stability analysis and enhancement of paralleled converters considering different current injection strategies," *IEEE Trans. Sustain. Energy*, vol. 13, no. 4, pp. 1957–1968, Oct. 2022.
[18] S. Huang, J. Yao, Y. Lin, and Y. Luo, "Interaction mechanism analysis and synchronization stability control for paralleled PLL-VSCs system during LVRT," in *Proc. IEEE Int. Conf. Power Sci. Technol.*, 2023, pp. 426–431.
[19] X. Fu, M. Huang, S. Pan, and X. Zha, "Cascading synchronization instability in multi-VSC grid-connected system," *IEEE Trans. Power Electron.*, vol. 37, no. 7, pp. 7572–7576, Jul. 2022.
[20] X. Li et al., "Nonlinear modeling and stability analysis of grid-tied paralleled-converters systems based on the proposed dual-iterative equal area criterion," *IEEE Trans. Power Electron.*, vol. 38, no. 6, pp. 7746–7759, Jun. 2023.
[21] M. G. Taul et al., "An efficient reduced-order model for studying synchronization stability of grid-following converters during grid faults," in *Proc. 20th Workshop Control Model. Power Electron.*, 2019, pp. 1–7.
[22] X. Li, Z. Tian, X. Zha, P. Sun, Y. Hu, and M. Huang, "An iterative equal area criterion for transient stability analysis of grid-tied converter systems with varying damping," *IEEE Trans. Power Syst.*, vol. 39, no. 1, pp. 1771–1784, Jan. 2024.
[23] D. Pal and B. K. Panigrahi, "Reduced-order modeling and transient synchronization stability analysis of multiple heterogeneous grid-tied inverters," *IEEE Trans. Power Del.*, vol. 38, no. 2, pp. 1074–1085, Apr. 2023.
[24] X. Fu, M. Huang, C. K. Tse, J. Yang, Y. Ling, and X. Zha, "Synchronization stability of grid-following VSC considering interactions of inner current loop and parallel-connected converters," *IEEE Trans. Smart Grid*, vol. 14, no. 6, pp. 4230–4241, Nov. 2023.
[25] Y. Yang et al., "The influence of wind farm group topology structure on power flow distribution," in *Proc. Int. Conf. Renewable Power Gener.*, 2015, pp. 1–5.
[26] W. Li, P. Chao, X. Liang, J. Ma, D. Xu, and X. Jin, "A practical equivalent method for DFIG wind farms," *IEEE Trans. Sustain. Energy*, vol. 9, no. 2, pp. 610–620, Apr. 2018.
[27] Technical Connection Rules for High-Voltage (VDE-AR-N 4120), 2015. [Online]. Available: https://www.vde.com/en/fnn/topics/technical-connection-rules/tar-for-high-voltage
[28] Requirements for Offshore Grid Connections in the Grid of TenneT TSO GmbH, Tennet, Amhem, The Netherlands, Dec. 2012.
[29] X. Wang, H. Wu, X. Wang, L. Dall, and J. B. Kwon, "Transient stability analysis of grid-following VSCs considering voltage-dependent current injection during fault ride-through," *IEEE Trans. Energy Convers.*, vol. 37, no. 4, pp. 2749–2760, Dec. 2022.
[30] Q. Hu, F. Ji, F. Ma, Y. Zhang, and L. Fu, "Matching analysis of LVRT grid code and injection current dependent voltage response of WTC connected to high impedance AC grid," *IEEE Trans. Energy Convers.*, vol. 37, no. 3, pp. 2236–2239, Sep. 2022.

Zhi Wang (Graduate Student Member, IEEE) received the B.Sc. and M.Sc. degrees in electrical engineering in 2020 and 2023, respectively, from Tianjin University, Tianjin, China, where he is currently working toward the Ph.D. degree in electrical engineering.

His current research interests include modeling, stability analysis, and control of power electronics dominated power systems.

Li Guo (Member, IEEE) received the B.Sc. and Ph.D. degrees in electrical engineering from South China University of Technology, Guangzhou, China, in 2002 and 2007, respectively.

He is currently a Full Professor with Tianjin University, Tianjin, China. His research interests include the optimal planning and design of microgrid, the coordinated operating strategy of microgrid, and the advanced energy management systems.

Xialin Li (Member, IEEE) received the B.Sc. and Ph.D. degrees in electrical engineering from Tianjin University, Tianjin, China, in 2009 and 2014, respectively.

In 2016, under the State Scholarship Fund, he was invited as a Visiting Professor to the Department of Electrical and Computer Engineering, University of Alberta, Edmonton, AB, Canada. Since 2018, he has been an Associate Professor with the School of Electrical Engineering and Automation, Tianjin University. His current research interests include the modeling and control of power converters, distributed generation, hybrid ac–dc microgrid, and multiterminal dc grids.

Zhongguan Wang (Member, IEEE) received the B.S. and Ph.D. degrees in electrical engineering from the Department of Electrical Engineering, Tsinghua University, Beijing, China, in 2014 and 2019, respectively.

He is currently an Associate Professor with the School of Electrical and Information Engineering, Tianjin University, Tianjin, China. His current research interests include operation of renewable power generation and active distribution system energy management.

Xiaodi Zang received the M.Sc. degree in electrical engineering from the Harbin Institute of Technology, Harbin, China, in 2008. She is currently working toward the D.Eng. degree in electrical engineering in Tianjin University, Tianjin, China.

Her current research interests include renewable energy generation grid-connected technology, and energy storage technology.

Jiebei Zhu (Senior Member, IEEE) received the B.Sc. degree in microelectronics from Nankai University, Tianjin, China, in 2008, and the M.Sc. and Ph.D. degrees in electronic and electrical engineering from the University of Strathclyde, Glasgow, U.K., in 2009 and 2013, respectively.

From 2013 to 2018, he acted as a Senior Power System Engineer and an Innovation Project Manager with National Grid Plc., Warwick and Wokinghan, U.K., of the GB transmission system operator. Since 2018, he has been a Professor with the Key Laboratory of Smart Grid of Ministry of Education, Tianjin University. He is also a Chartered Engineer with the U.K. Royal Engineering Council, London, U.K. His research interests involve HVdc transmission system control, renewable energy systems, and energy storage technologies.

Xu Zhou received the M.Sc. degree in electrical engineering from North China University of Technology, Beijing, China, in 2019. He is currently working toward the Ph.D. degree in School of Electrical and information Engineering, Tianjin University, Tianjin, China.

His current research interests include modeling, control, and stability analysis of the grid-forming converters and grid-following converters.

Chengshan Wang (Senior Member, IEEE) received the B.Sc., M.Sc., and Ph.D. degrees in electrical engineering from Tianjin University, Tianjin, China, in 1983, 1985, and 1991, respectively.

He became a Full Professor with Tianjin University in 1996. He was a Visiting Scientist with Cornell University, Ithaca, NY, USA, from1994 to 1996, and a Visiting Professor with Carneigie Mellon University, Pittsburgh, PA, USA, from 2001 to 2002. He was the Chief Scientist of the 973 Project Research on the Key Issues of Distributed Generation Systems from 2009 to 2013 that was participated by Chinese power engineering scientists from eight leading institutions. His research interests include the area of distribution system analysis and planning, distributed generation system and microgrid, and power system security analysis.

Dr. Wang is the gainer of the Fok Ying Tung Fund, the Excellent Young Teacher Fund of Education Ministry, and a winner of the National Science Fund for Distinguished Young Scholars.